Acoustic Travel-Time Tomography for Wind Energy

Nicholas Hamilton and Emina Maric

National Renewable Energy Laboratory

NREL is a national laboratory of the U.S. Department of Energy
Office of Energy Efficiency & Renewable Energy
Operated by the Alliance for Sustainable Energy, LLC

This report is available at no cost from the National Renewable Energy Laboratory (NREL) at www.nrel.gov/publications.

Contract No. DE-AC36-08GO28308

Technical Report
NREL/TP-5000-84388
December 2022

Acoustic Travel-Time Tomography for Wind Energy

Nicholas Hamilton and Emina Maric

National Renewable Energy Laboratory

Suggested Citation

Hamilton, Nicholas, and Emina Maric. 2022. *Acoustic Travel-Time Tomography for Wind Energy*. Golden, CO: National Renewable Energy Laboratory. NREL/TP-5000-84388. https://www.nrel.gov/docs/fy23osti/84388.pdf.

NREL is a national laboratory of the U.S. Department of Energy
Office of Energy Efficiency & Renewable Energy
Operated by the Alliance for Sustainable Energy, LLC

This report is available at no cost from the National Renewable Energy Laboratory (NREL) at www.nrel.gov/publications.

Contract No. DE-AC36-08GO28308

Technical Report
NREL/TP-5000-84388
December 2022

National Renewable Energy Laboratory
15013 Denver West Parkway
Golden, CO 80401
303-275-3000 • www.nrel.gov

NOTICE

This work was authored by the National Renewable Energy Laboratory, operated by Alliance for Sustainable Energy, LLC, for the U.S. Department of Energy (DOE) under Contract No. DE-AC36-08GO28308. Funding provided by the U.S. Department of Energy Office of Energy Efficiency and Renewable Energy Wind Energy Technologies Office. The views expressed herein do not necessarily represent the views of the DOE or the U.S. Government.

Cover Photos by Dennis Schroeder: (clockwise, left to right) NREL 51934, NREL 45897, NREL 42160, NREL 45891, NREL 48097, NREL 46526.

NREL prints on paper that contains recycled content.

Executive Summary

New remote sensing technologies for directly observing atmospheric flow in the proximity of operating wind turbines are necessary to advance wind turbine design, wind plant control, and for the validation of high-fidelity numerical models—fundamental goals of the Atmosphere to Electrons program sponsored by the U.S. Department of Energy's Wind Energy Technologies Office. Modern remote sensing technologies for commercial and research applications rely on the backscatter of light or sound waves, which limits spatial and temporal resolution and cannot produce reliable flow estimates near solid bodies or reflective surfaces. Acoustic tomography (AT) is an innovative sensing technology based on the fundamental thermodynamic and mechanical properties of the atmosphere and an inverse algorithm that can reconstruct both velocity and temperature fields within a network of acoustic transducers. AT relies on the direct travel path of acoustic signals between speakers and microphones in the network and can achieve much higher resolutions than conventional backscatter technologies. For wind energy research and development applications, AT offers a promising path forward for high-resolution measurements, integrating well-founded mathematical methods with mature and commonly available acoustic and signal processing hardware. This report provides an update on the development of the AT array on the National Renewable Energy Laboratory's (NREL's) Flatirons Campus and includes a brief review of the instrumentation, characterization of the measurement system, signal processing, and resulting flow field estimates. Designs for future AT systems and applications are detailed in this report, including applications for utility-scale wind turbines, summaries of new capabilities, and engineering and theoretical challenges, which help to outline future directions for AT technology research and development at NREL. Developing AT as a remote sensing technology will establish it as a transformational remote sensing technique that represents a significant advance in measurement instrumentation, enabling new fundamental insights into the structure of the atmospheric boundary layer and supporting applications for wind energy, pollutant transport, and resource characterization.

List of Acronyms

A2e	Atmosphere to Electrons
ABL	atmospheric boundary layer
AT	acoustic tomography
DOE	U.S. Department of Energy
Hz	hertz
K	Kelvin
kHz	kilohertz
LES	large-eddy simulation
m	meter
min.	minute
ms	millisecond
NMSE	normalized mean square error
NREL	National Renewable Energy Laboratory
PoF	power over fiber
s	second
STD	standard deviation
TDSI	time-dependent stochastic inversion
UAS	uncrewed aerial system

Table of Contents

List of Figures

List of Tables

1 Introduction

Understanding the complex turbulent flow between and around wind turbines is critical for optimizing wind plant design and operation and is one of the primary focus areas of the Atmosphere to Electrons (A2e) program sponsored by the U.S. Department of Energy's (DOE's) Wind Energy Technologies Office. While advanced numerical models of wind plant flows have matured exponentially in the last decade, the observational technology required to validate these models and verify important physical processes has advanced more slowly. Observational capability for aerodynamic research of wind turbines, wind plants, and wakes is limited by current remote sensing technology, both in terms of measurement resolution and cost of instrumentation. The leading remote sensing technology for wind energy and atmospheric research comes in the form of scanning lidar (light detection and ranging) or radar (Mann et al. 2010; Iungo and Porté-Agel 2014; Aitken and Lundquist 2014; Herges et al. 2017; Schroeder, Hirth, and Guynes 2017). Both technologies rely on the backscatter of emitted radiation (infrared light and radio waves for lidar and radar, respectively) toward the source of the emission, fundamentally limiting the resolutions of both technologies and providing only scalar, line-of-sight observations. Resolving velocity vector components requires either the use of multiple instruments (multi-Doppler scanning) or strong assumptions relating velocity fluctuations in the streamwise, transverse, and vertical directions. In addition, scanning lidar and radar observations are convolved with a Lorenz weighting function and integrate small-scale fluctuations over an averaging volume that depends on the distance from the source/receiver. Despite the tremendous advances that scanning lidar and radar have offered to atmospheric science and wind energy research, they are not able to make fast, reliable measurements with the spatial resolution required to validate theoretical and computational models.

Acoustic tomography (AT) is a remote sensing technique that represents a transformational advance in measurement technology and will help advance the goals of A2e and the wind industry as a whole. AT provides a method for investigating the dynamic processes behind multidimensional turbulent structures, validating atmospheric models, and observing near-surface momentum and heat fluxes. This has profound implications for the study of engineering flows and climatology. Simultaneous realizations of turbulent velocity and temperature fields over a multidimensional spatial and temporal domain are not possible with any other currently available remote sensing technology. The AT array shown in Figure 1, installed and validated at the National Renewable Energy Laboratory's (NREL's) Flatirons Campus is a unique facility for wind energy and atmospheric science research. The AT array facility at the Flatirons Campus complements NREL's observational capability available for DOE and wind energy industry research, enabling new scientific insights, new partnerships, and further helping NREL satisfy A2e validation and field research objectives.

This report reviews the underlying theory behind AT, including the methods used to estimate the bulk flow quantities as well as the time-dependent stochastic inversion (TDSI) in Section 2. In Section 3, we introduce the current design of the AT array at NREL, including details of the data processing, system calibration, applications and system limitations. Section 4 presents some results obtained from the NREL AT array. Section 5 contains an extensive discussion on future acoustic tomography array configurations and capabilities at NREL. A flowchart is included for reference in Figure 2. It highlights the four critical stages of AT: (1) signal emission/detection, (2) travel time detection, (3) mean field estimation, (4) fluctuating field estimation. Each step references the appropriate equations as necessary.

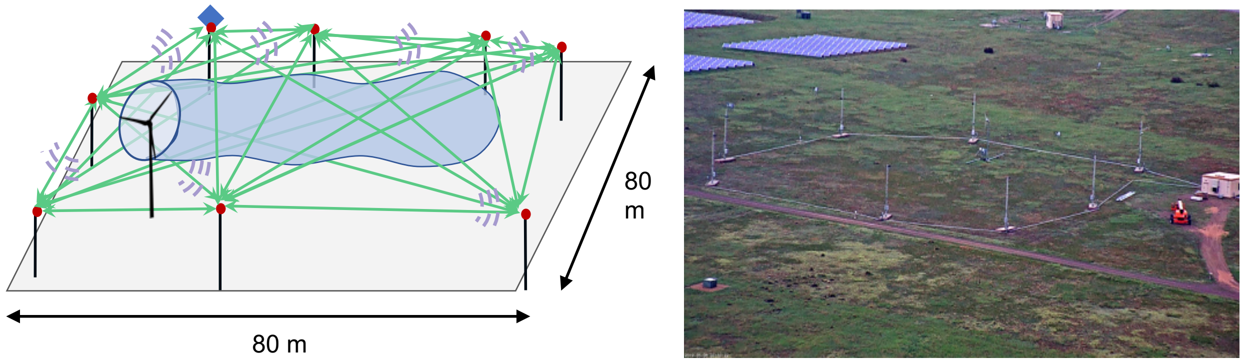

Figure 1. The acoustic tomography array at Flatirons Campus, including a subscale wind turbine. Red dots indicate acoustic transducer placement, and the blue diamond indicates the sonic anemometer and temperature/humidity probe.

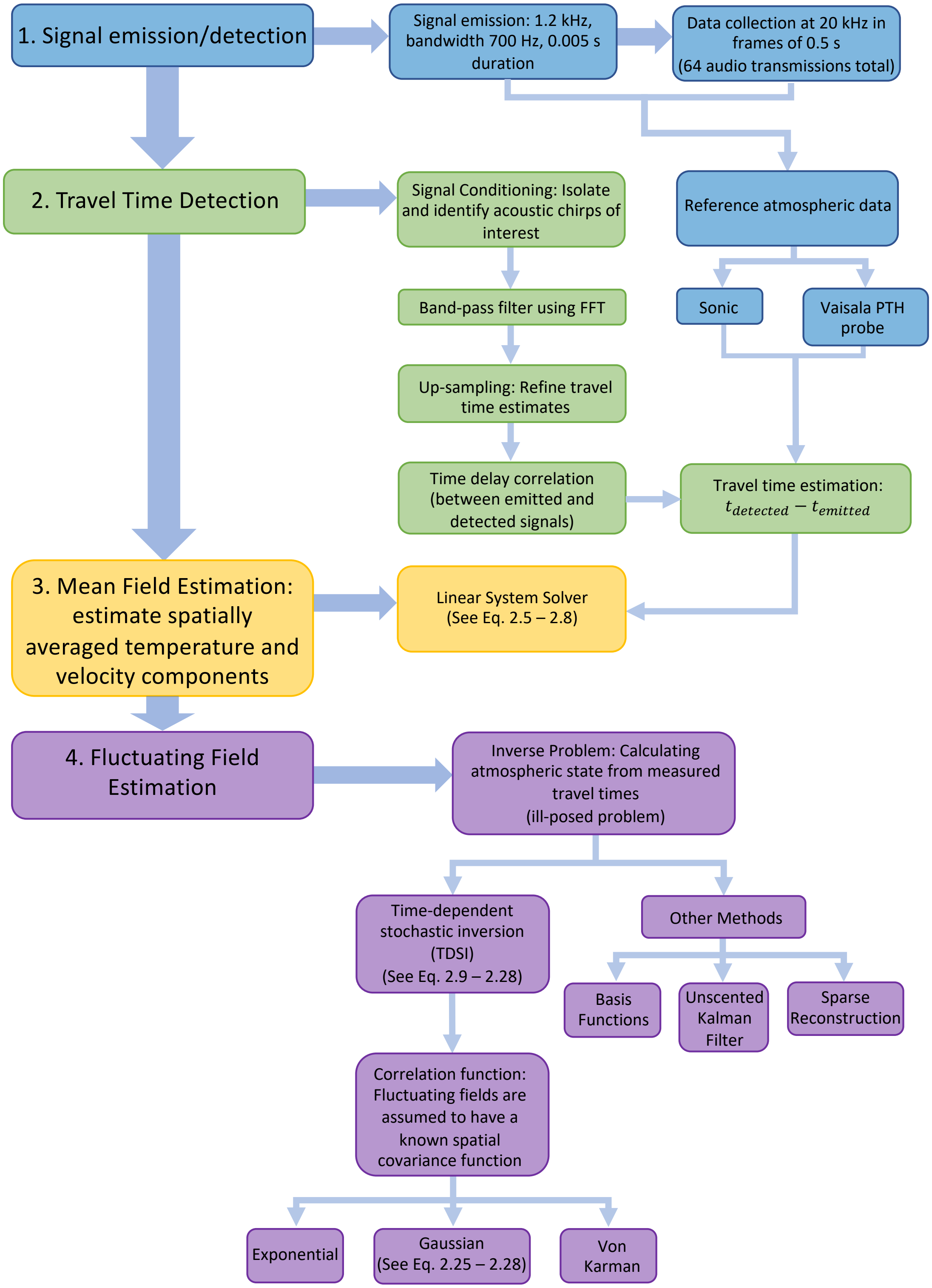

Figure 2. A flowchart of the AT methodology/processes at NREL.

2 Theory

The basis of acoustic tomography explored here follows the formulation provided in Vecherin et al. (2006). The theory builds from an assumption that the travel time (t_i) of any acoustic signal through the atmosphere depends only on the length of the path traversed along the i^{th} ray and the group velocity of the acoustic signal, u_i, which is the sum of the local speed of sound and the projection of the ambient convection velocity onto the unit vector aligned with the path $\boldsymbol{r}_i$. The travel time, t_i, along any signal path, L_i, can be expressed

$$t_i = \int_{L_i} \frac{1}{u_i(\boldsymbol{r}_i)} dl \tag{2.1}$$

where $i = 1, \ldots, I$ represents the index of the path and I is the total number of travel paths considered ($I = 64$ for the current application) . The local speed of sound is typically taken as the Laplace adiabatic sound speed, c_L, which is related to the acoustic virtual temperature, T_{av},

$$c_L = \sqrt{\gamma R_a T_{\text{av}}} \tag{2.2}$$

where $\gamma \approx 1.41$ is the ratio of specific heats and $R_a = 287.058$ is the universal gas constant for dry air.

Decomposing the instantaneous fields of the speed of sound, temperature, and ambient atmospheric horizontal velocity components (c_L, T_{av}, $\tilde{u}$, and $\tilde{v}$, respectively) into spatially averaged values (denoted with the 0 subscript) and spatially heterogeneous fluctuations ($c, T, u, v = f(\boldsymbol{r}, t)$) yields

$$\begin{aligned} c_L(\boldsymbol{r},t) &= c_0(t) + c(\boldsymbol{r},t) \\ T_{\text{av}}(\boldsymbol{r},t) &= T_0(t) + T(\boldsymbol{r},t) \\ \tilde{u}(\boldsymbol{r},t) &= u_0(t) + u(\boldsymbol{r},t) \\ \tilde{v}(\boldsymbol{r},t) &= v_0(t) + v(\boldsymbol{r},t). \end{aligned} \tag{2.3}$$

Here, $\tilde{u}(\boldsymbol{r},t)$ and $\tilde{v}(\boldsymbol{r},t)$ are the components of the two-dimensional velocity vector and $\boldsymbol{r}$ represents the Cartesian coordinates of the locations within the tomographic area.

The linearized expression for travel time of an acoustic emission is

$$t_i = \varepsilon_i(t_0) + \frac{L_i}{c_0(t)}\left(1 - \frac{u_0(t)\cos\,\phi_i + v_0(t)\sin\,\phi_i}{c_0(t)}\right) - \frac{1}{c_0^2(t)}\int_{L_i} \frac{c_0(t)}{2T_0(t)} T(\boldsymbol{r},t) + u(\boldsymbol{r},t)\cos\,\phi_i + v(\boldsymbol{r},t)\sin\,\phi_i \; dl, \tag{2.4}$$

where $\varepsilon_i(t_0)$ is the noise in the travel time and ϕ_i is the angle between the i^{th} ray and the positive x axis.

2.1 Mean Field Estimation

Estimates of the mean (spatially averaged) temperature and in-plane components of velocity (T_0, u_0, and v_0) are achieved by assuming a spatially homogeneous field. With this assumption, Equation (2.4) reduces to

$$t_i = \frac{L_i}{c_0(t)}\left(1 - \frac{u_0(t)\cos\,\phi_i + v_0(t)\sin\,\phi_i}{c_0(t)}\right) \tag{2.5}$$

Equation (2.5) can then be rewritten in matrix form:

$$\boldsymbol{G}\boldsymbol{f} = \boldsymbol{b} \tag{2.6}$$

where the elements of the column vector $\boldsymbol{b}$ are known and are given by $b_i = t_i(t)/L_i$. The vector of unknown values has three elements, $\boldsymbol{f} = [1/c_0(t), u_0(t)/c_0^2(t), v_0(t)/c_0^2(t)]$, and the matrix $\boldsymbol{G}$ is a function of the orientation of each path vector with respect to the positive x-axis, oriented east-west in the current AT array:

$$\boldsymbol{G} = \begin{bmatrix} 1 & -\cos\,\phi_1 & -\sin\,\phi_1 \\ \vdots & \vdots & \vdots \\ 1 & -\cos\,\phi_I & -\sin\,\phi_I \end{bmatrix} \tag{2.7}$$

The observed travel times of acoustic chirps along the paths r_i provide an overdetermined linear system for the spatially averaged speed of sound and convective velocity. Least-squares estimation resolves the components of $\boldsymbol{f}$ as

$$\boldsymbol{f} = (\boldsymbol{G}^T\boldsymbol{G})^{-1}\boldsymbol{G}^T\boldsymbol{b} \tag{2.8}$$

resulting in estimates of $c_0(t)$, $u_0(t)$, and $v_0(t)$ at the temporal resolution of frame collection by the AT system—in this case, 2 hertz (Hz).

2.2 Time-Dependent Stochastic Inversion

Once the spatial mean values of temperature, adiabatic sound speed, and wind velocity fields within a tomographic area are known, the column vector of data $d(t)$ obtained at time t with elements is introduced as

$$d_i(t) = L_i[c_0(t) - u_0(t)\cos\phi_i - v_0(t)\sin\phi_i] - c_0^2(t)t_i(t) + \xi_i(t) \tag{2.9}$$

where the noise term $\xi_i(t)$ includes errors in travel time measurement $\varepsilon_i(t)$ and errors in estimation of the associated spatially averaged temperature and velocity. Using Equation (2.4), the data vector can be expressed as $\boldsymbol{d}(t) = \boldsymbol{d}_0(t) + \boldsymbol{\xi}(t)$, where $\boldsymbol{d}_0(t)$ is a vector of noise-free data expressed as

$$d_{0i}(t) = \int_{L_i}\left(\frac{c_0(t)}{2T_0(t)}T(\boldsymbol{r},t) + u(\boldsymbol{r},t)\cos\phi_i + v(\boldsymbol{r},t)\sin\phi_i\right)dl. \tag{2.10}$$

The central problem of time-dependent stochastic inversion is to reconstruct the fluctuating fields of temperature and velocity, $T(\boldsymbol{r},t_0)$, $u(\boldsymbol{r},t_0)$, and $v(\boldsymbol{r},t_0)$, at a time t_0 with knowledge of the acoustic travel time and the spatial average temperature and velocity. This is undertaken through the introduction of a vector of models ($\boldsymbol{m}$) for temperature and velocity at all measurement times along all paths:

$$\boldsymbol{m}(t_0) = [T(\boldsymbol{r}_1,t_0)\ ;\ \dots\ ;\ T(\boldsymbol{r}_J,t_0)\ ;\ u(\boldsymbol{r}_1,t_0)\ ;\ \dots\ ;\ u(\boldsymbol{r}_J,t_0)\ ;\ v(\boldsymbol{r}_1,t_0)\ ;\ \dots\ ;\ v(\boldsymbol{r}_J,t_0)], \tag{2.11}$$

where J is the number of spatial locations within the domain to be resolved. Assuming that one can collect data $N+1$ times during a time interval with duration τ, denoted as N_τ, by emitting and detecting chirps within the tomographic area, one can form the vector $\boldsymbol{d}$ for each frame

$$\boldsymbol{d} = [\boldsymbol{d}(t-N\tau)\ ;\ \boldsymbol{d}(t-N\tau+\tau)\ ;\ \dots\ ;\ \boldsymbol{d}(t)]\,. \tag{2.12}$$

Here, $\boldsymbol{d}$ is a vector containing $(N+1)$ column vectors $\boldsymbol{d}(t-n\tau)$, each of length I, and $n = 0,1...,N$. τ represents equal time intervals at which data is collected.

Using the data vectors from Equation (2.12), it is necessary to find a linear estimate $\hat{\boldsymbol{m}}(t_0)$ of the unknown models $\boldsymbol{m}(t_0)$ at each time t_0. Models are formed using observed travel times ahead of ($t_0 > t$), concurrent with ($t_0 = t$), or following ($t_0 < t$) any time of interest, t_0. In the current formulation, models are sought as linearizations of the observed data:

$$\hat{\boldsymbol{m}}(t_0) = \boldsymbol{A}\boldsymbol{d}, \tag{2.13}$$

where the elements of matrix $\boldsymbol{A}$ are unknown and must be estimated. Matrix $\boldsymbol{A}$ contains linear coefficients a_{jk}, where $j = 1,2,\dots,3J$ and $k = 1,2,\dots,(N+1)I$. Discrepancies $\boldsymbol{\varepsilon}$ between the true and reconstructed temperature and velocity fields at time t_0 are written as

$$\boldsymbol{\varepsilon}_j = \hat{\boldsymbol{m}}_j(t_0) - \boldsymbol{m}_j(t_0). \tag{2.14}$$

Elements of the coefficient matrix $\boldsymbol{A}$ are chosen to minimize discrepancies $\boldsymbol{\varepsilon}_j$ in a mean-squared sense.

The matrix $\boldsymbol{A}$ that solves the problem does not depend on a particular structure of the models $\boldsymbol{m}$ and data $\boldsymbol{d}$:

$$\boldsymbol{A} = \boldsymbol{R_{md}}\boldsymbol{R_{dd}}^{-1}, \tag{2.15}$$

where $\boldsymbol{R_{md}}$ and $\boldsymbol{R_{dd}}$ are model-data and data-data covariance matrices. Since data and models have been chosen, covariance matrices have the following structure:

$$\boldsymbol{R_{md}} = [\boldsymbol{B_{md}}(t_0,t-N\tau),\ \boldsymbol{B_{md}}(t_0,t-N\tau+\tau),\ \dots,\ \boldsymbol{B_{md}}(t_0,t)] \tag{2.16}$$

$$\boldsymbol{R_{dd}} = \begin{bmatrix} \boldsymbol{B_{dd}}(t-N\tau,t-N\tau) & \boldsymbol{B_{dd}}(t-N\tau,t-N\tau+\tau) & \dots & \boldsymbol{B_{dd}}(t-N\tau,t) \\ \boldsymbol{B_{dd}}(t-N\tau+\tau,t-N\tau) & \boldsymbol{B_{dd}}(t-N\tau+\tau,t-N\tau+\tau) & \dots & \boldsymbol{B_{dd}}(t-N\tau+\tau,t) \\ \vdots & \vdots & \ddots & \vdots \\ \boldsymbol{B_{dd}}(t,t-N\tau) & \boldsymbol{B_{dd}}(t,t-N\tau+\tau) & \dots & \boldsymbol{B_{dd}}(t,t) \end{bmatrix} \tag{2.17}$$

Here, $\boldsymbol{B_{md}}(t_1,t_2) = \langle \boldsymbol{m}(t_1)\boldsymbol{d}^T(t_2)\rangle$ is a covariance matrix of size $[3J, I]$ between the models at time t_1 and the data at time t_2. Similarly, $\boldsymbol{B_{dd}}(t_1,t_2) = \langle \boldsymbol{d}(t_1)\boldsymbol{d}^T(t_2)\rangle$ is the covariance matrix of size $[I, I]$ between the data at times t_1 and t_2. Note that the matrix $R_{\boldsymbol{dd}}$ is symmetric by definition. It is further possible to quantify error in the field reconstruction process directly as

$$\boldsymbol{R}_{\varepsilon\varepsilon} = \boldsymbol{R_{mm}} - \boldsymbol{R_{md}}\boldsymbol{R_{dd}^{-1}}\boldsymbol{R_{md}^{T}}, \tag{2.18}$$

where $\boldsymbol{R_{mm}} = \langle \boldsymbol{m}(t_0)\boldsymbol{m}^T(t_0)\rangle$ represents the covariance of the models at time t_0.

Since the optimal stochastic inverse operator $\boldsymbol{A}$ given by Equation (2.15) is determined in terms of the matrices $\boldsymbol{R_{md}}$ and $\boldsymbol{R_{dd}}$, the formulation of each covariance matrix determines the fidelity and accuracy of the reconstructed temperature and velocity fields. In the case of travel-time tomography, one can use the linear relationship expressed in Equation (2.9) to derive expressions for the covariance matrix $\boldsymbol{B_{md_0}}(t_1,t_2)$ between the models at time t_1 and the noise-free data at time t_2:

$$\begin{aligned}
\boldsymbol{B_{m_j d_{0i}}}(t_1,t_2) &= \langle m_j(t_1) d_{0i}(t_2)\rangle && (2.19)\\
&= \int_{L_i} \left(\frac{c_0(t_2)}{2T_0(t_2)} \langle m_j(t_1) T(\boldsymbol{r},t_2)\rangle + \langle m_j(t_1) u(\boldsymbol{r},t_2)\rangle \cos\phi_i + \langle m_j(t_1) v(\boldsymbol{r},t_2)\rangle \sin\phi_i \right) dl && (2.20)\\
&= \begin{cases}
\int_{L_i} \left(\frac{c_0(t_2)}{2T_0(t_2)} B_{TT}(\boldsymbol{r}_j,t_1;\boldsymbol{r},t_2) \right) dl, & \text{if } 1 \le j \le J\\
\int_{L_i} \left(B_{uu}(\boldsymbol{r}_j,t_1;\boldsymbol{r},t_2)\cos\phi_i + B_{uv}(\boldsymbol{r}_j,t_1;\boldsymbol{r},t_2)\sin\phi_i \right) dl, & \text{if } J+1 \le j \le 2J\\
\int_{L_i} \left(B_{vu}(\boldsymbol{r}_j,t_1;\boldsymbol{r},t_2)\cos\phi_i + B_{vv}(\boldsymbol{r}_j,t_1;\boldsymbol{r},t_2)\sin\phi_i \right) dl, & \text{if } 2J+1 \le j \le 3J
\end{cases} && (2.21)
\end{aligned}$$

Note that the index j indicates which field (either temperature, T, x-velocity, u, or y-velocity, v) is being considered, and that there are J instances of each respective model. Indices $i = 1,\ldots,I$ indicate the index of the path being considered and $\boldsymbol{r} \in L_i$ are the path vectors. Spatial-temporal covariance functions of the corresponding fields are denoted B_{TT}, B_{uu}, B_{uv}, B_{vu}, and B_{vv}, and $\boldsymbol{r}_j$ are the chosen spatial points within the tomographic area for which the sought fields are reconstructed.

Similarly, the covariance matrix $\boldsymbol{B_{d_0 d_0}}(t_1,t_2)$ between the noise-free data at two times is provided by the expression

$$\begin{aligned}
\boldsymbol{B_{d_{0i} d_{0p}}}(t_1,t_2) = \iint_{L_i,L_p} & \frac{c_0(t_1)c_0(t_2)}{4T_0(t_1)T_0(t_2)} B_{TT}(\boldsymbol{r},t_1;\boldsymbol{r}',t_2) + B_{uu}(\boldsymbol{r},t_1;\boldsymbol{r}',t_2)\cos\phi_i\cos\phi_p +\\
& B_{vv}(\boldsymbol{r},t_1;\boldsymbol{r}',t_2)\sin\phi_i\sin\phi_p + B_{uv}(\boldsymbol{r},t_1;\boldsymbol{r}',t_2)\cos\phi_i\sin\phi_p + B_{vu}(\boldsymbol{r},t_1;\boldsymbol{r}',t_2)\sin\phi_i\cos\phi_p \, dl \, dl',
\end{aligned} \tag{2.22}$$

where indices $i, p = 1,\ldots,I$ both indicate which paths are being considered and $\boldsymbol{r} \in L_i, \boldsymbol{r}' \in L_p$ are the path vectors. Note that it is assumed that the covariance functions between the temperature and either component of velocity $B_{Tu} = B_{Tv} = 0$.

With a further assumption that the fluctuating temperature and velocity are stationary, the covariance fields lose their explicit dependence on either of the times being considered, and instead rely only on the time separation

$$B(\boldsymbol{r},t_1;\boldsymbol{r}',t_2) \Rightarrow B(\boldsymbol{r},\boldsymbol{r}',\Delta t), \qquad \Delta t = t_2 - t_1. \tag{2.23}$$

Employing Taylor's frozen field hypothesis, one can assume that the fluctuating field does not evolve in time but is simply convected along the main flow direction at some advection velocity $\boldsymbol{U}$. Thus the formulation of the covariance functions may be further simplified as

$$B(\boldsymbol{r},\boldsymbol{r}',\Delta t) \Rightarrow B^S(\boldsymbol{r},\boldsymbol{r}' - \boldsymbol{U}\Delta t), \tag{2.24}$$

where the superscript S implies that the covariance function is now purely spatial, and all time dependence of the function has been removed.

Finally, to describe the spatial covariance of the temperature and wind velocity fields within the tomographic area, the following Gaussian covariance functions were used:

$$B^S_{TT} = \sigma_T^2 \exp\left(-\frac{(\boldsymbol{r}-\boldsymbol{r}')^2}{l_T^2}\right), \tag{2.25}$$

$$B^S_{uu} = \sigma_u^2 \exp\left(-\frac{(\boldsymbol{r}-\boldsymbol{r}')^2}{l^2}\right)\left(1-\frac{(y-y')^2}{l^2}\right), \tag{2.26}$$

$$B^S_{vv} = \sigma_v^2 \exp\left(-\frac{(\boldsymbol{r}-\boldsymbol{r}')^2}{l^2}\right)\left(1-\frac{(x-x')^2}{l^2}\right), \tag{2.27}$$

$$B^S_{uv} = \sigma_u\sigma_v \exp\left(-\frac{(\boldsymbol{r}-\boldsymbol{r}')^2}{l^2}\right)\left(\frac{(x-x')(y-y')}{l^2}\right), \tag{2.28}$$

where σ_T, σ_u, and σ_v are the standard deviations of the corresponding fields, l_T and l are correlation lengths of temperature and velocity, and the vectors $\boldsymbol{r} = (x, y)$ and $\boldsymbol{r}' = (x', y')$. With the correlation functions in Equations (2.25) and (2.26), one can estimate the covariance matrices $\boldsymbol{R}_{\boldsymbol{md}_0}$ and $\boldsymbol{R}_{\boldsymbol{d}_0\boldsymbol{d}_0}$, and finally the coefficient matrix $\boldsymbol{A}$ using Equation (2.15). In the described TDSI algorithm, five parameters must be chosen or deduced: σ_T, σ_u, σ_v, l_T, and l. All parameters may be estimated from the sonic anemometer installed on Station 8 of the AT array. Note that the formulation in Equations (2.25) and (2.26) employ a Gaussian description of the covariance for temperature and velocity fields. Other formulations may be more physically representative of the field variance in the atmospheric boundary layer but may come at increased computational costs.

3 Acoustic Tomography Array Design

The AT array in its current design resolves fluctuating temperature and velocity fields in a plane parallel to the ground. The fundamental operating principle of AT is that the time of flight of an acoustic signal through the atmosphere depends on the distance between emission and reception sites and on the local group velocity. The speed of sound in turn depends on the thermodynamic state of the atmosphere, described by the ratio of specific heats, the universal gas constant, and the acoustic virtual temperature, T. Estimating the travel time of an acoustic signal, or chirp, from the local atmospheric state is known as the *forward* problem.

The *inverse* problem seeks the atmospheric state from measured travel times, which is an ill-posed problem. The solution to the inverse problem can be estimated with a highly overdetermined linear system describing the heterogeneous velocity and temperature fields in terms of their effects on the travel time of a series of acoustic signals. Reconstructing the turbulent temperature and velocity fields through TDSI relies on an assumed Gaussian covariance model for velocity and temperature fluctuations in space in order to estimate u, v, and T within the interrogation area.

3.1 System Design

The AT array at NREL has been used to demonstrate viability of the method in a two-dimensional (2D) configuration (Vecherin, Ostashev, and Wilson 2008; Ostashev et al. 2008) with all speakers and microphones in co-located pairs in a plane parallel to the ground. The AT array located at Site 1E at the NREL Flatirons Campus (shown in Figures 1 and 3) consists of a control center, which houses the data acquisition system and processing computer, and eight towers that support speakers and microphones. Speaker and microphone locations within the array were precisely measured through a total station theodolite survey. Figure 3 also shows the arrangement of acoustic transducers in the AT array at NREL. They are arranged along the boundary of an 80-m × 80-m square with the propagation vectors of acoustic chirps sent between each pair of towers.

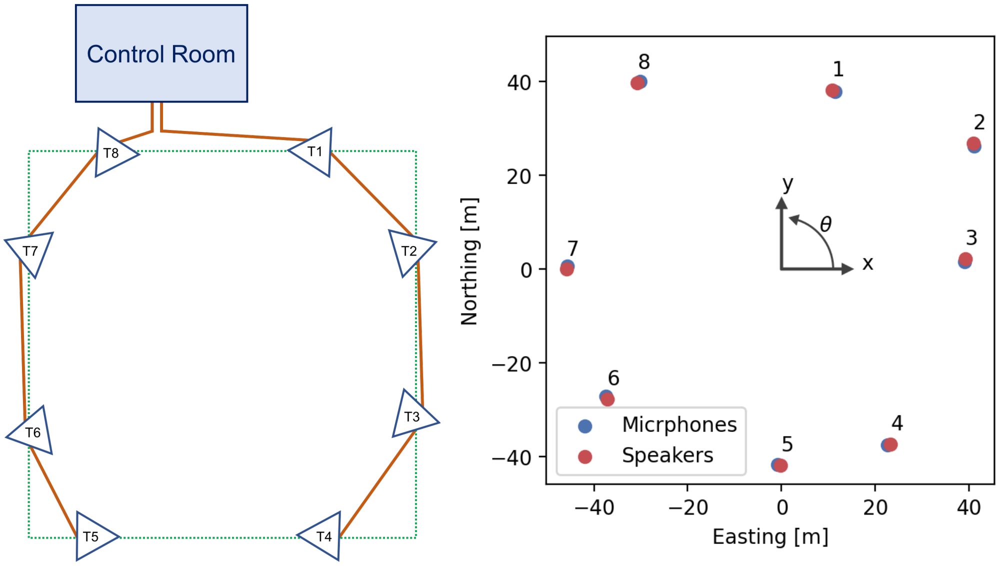

Figure 3. AT array schematics representing (left) control room and tower locations (labeled triangles) and (right) acoustic transducer locations.

Acoustic chirps are emitted through a set of eight speakers located on the towers. All chirps in the current system design are identical (1.2-kilohertz [kHz] central frequency, 700-Hz half bandwidth, 0.005-s duration) and were designed to fit in the spectral range that is least attenuated by the atmosphere. Speakers emit chirps every half-second (2 Hz) and are offset in time such that the chirps from each speaker do not overlap in the microphone recordings.

Microphones used in the AT array are B&K UA1-1404 outdoor microphones and SM PR8 preamplifiers. The selected mic/preamp combination is rated to perform in outdoor environments and should have no problems with the full range of operating and weather conditions present at the Flatirons Campus in Colorado. This is especially advantageous considering that the wind season at the NREL Flatirons Campus is roughly from October to May and can experience cold/icy/wet conditions (Hamilton and Debnath 2019).

3.2 Data Processing

AT data are recorded in "frames" lasting 0.5 s. Each frame contains a single chirp, emitted by the speakers on the eight station towers, each of which is recorded by the eight microphones. In total, 64 audio transmissions are recorded along paths connecting each speaker to each microphone. In practice, transmissions between speakers and microphones at the same station are not considered in the estimation of flow and temperature fields. Chirps emitted by each speaker are offset in time by approximately 0.04 s to ease the identification of source/detection pairs. All chirps are emitted within 0.2 s of the beginning of a frame. The longest signal travel time diagonally across the array is approximately 0.28 s, ensuring that all chirps are sent and received within the 0.5 s duration of a single frame. Frames are designed to allow all signals to propagate throughout the transmission area entirely before starting a new frame. Signal propagation directions are depicted in Figure 4.

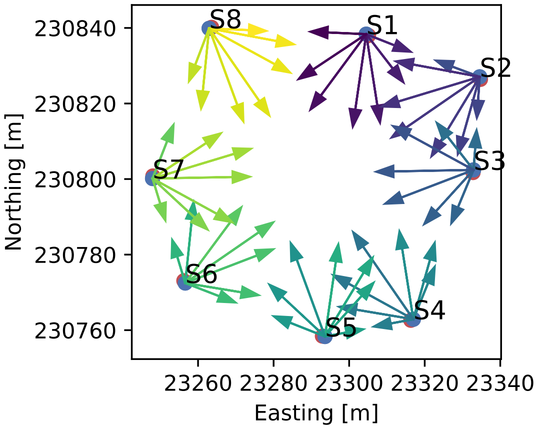

Figure 4. Signal propagation directions from each of the eight stations.

The detection of acoustic travel times shown in Figure 5 is a central challenge of the hardware side of the AT system. The expected travel time, t_{expected}, of each signal depends on the path traveled, L_i, and the thermodynamic state of the atmosphere as contained in the group velocity $\boldsymbol{u}_{gr}$. The observed travel time, t_{detected}, feeds into the estimation of the background mean atmospheric state. Finally, the difference between t_{expected} and the t_{detected} is ultimately used to estimate the fluctuating temperature and velocity fields.

3.2.1 Data Collection

Raw acoustic data are recorded at 20 kHz by all eight microphones constituting the array. Signals used to drive the speakers are also written simultaneously to microphone recordings to complete the audio portion of the data. In parallel to the audio recording, reference atmospheric data are recorded by a sonic anemometer and Vaisala pressure/temperature/humidity probe located at the top of Station 8. Auxiliary data contain channels of reference speed of sound and three Cartesian components of velocity, temperature, and humidity recorded at 20 Hz. Auxiliary data channels are described in Table 1.

3.2.2 Signal Conditioning

Raw microphone signals represent all frequencies within the range of the microphone, subject to its own response curve (flat frequency response in the audible range). In addition to the acoustic chirps emitted by the speakers, the signals recorded directly by the microphones contain ambient wind noise as well as any other acoustic signals in the area, such as passing vehicles and HVAC or compressor noise. Isolating and identifying the acoustic chirps of interest is facilitated by filtering the signals to the frequency band representative of the designed chirp.

The acoustic chirp used in the AT array has a central frequency of 1.2 kHz, a bandwidth of 700 Hz, and a duration of 0.005 s. Emitted chirps differ from their design by virtue of being generated by a driver and emitted through

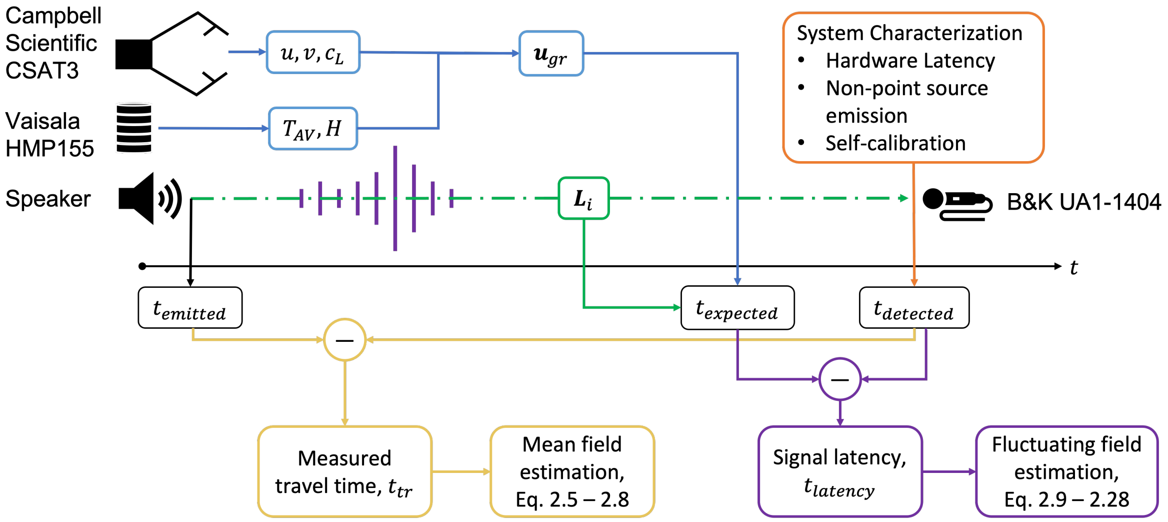

Figure 5. Schematic depicting travel time of acoustic chirps, expected/detected signal arrival time, and connections to field estimation.

Table 1. Channels reported by the CSAT3 sonic anemometer and Vaisala T/H probe at station 8

Channel	Unit	Description
u_x	m/s	horizontal (x) component of velocity
u_y	m/s	horizontal (y) component of velocity
u_z	m/s	vertical (z) component of velocity
c	m/s	local speed of sound
T	K	local temperature
H	%	local relative humidity

the speaker cone, and then traveling through the atmosphere, all of which modulate the chirp's frequency content and amplitude. Accordingly, the chirps received by the microphones often differ significantly from their respective nominal design.

Amplitude and frequency modulation incurred during emission and travel serve to obscure the chirps in the microphone data. A first step in signal conditioning is to apply a band-pass filter that removes ambient acoustic signals and mitigates unwanted frequencies in the recorded chirps. Figure 6 compares the designed chirp used to drive the speaker to an example of a chirp received by a microphone. Filtering is accomplished by applying a fast Fourier transform to each raw microphone signal and setting the amplitudes of any frequency more than two times the chirp bandwidth to zero. Filtering using a "hard" band-pass limit as done here introduces convolution error in the form of ringing to the resultant audio time series, but does not interfere with signal detection. Many methods that optimize the filtered signal in terms of minimizing convolution error introduce additional time delays that are not easily accounted for. Given that the precise resolution of travel times is paramount to flow and temperature field estimation, it is preferable to introduce convolution error to the signal than to introduce additional time delays. Alternate frequency filtering methods have been explored in the context of acoustic tomography signal processing but have not been implemented in the current work to mitigate the introduction of time-lag issues.

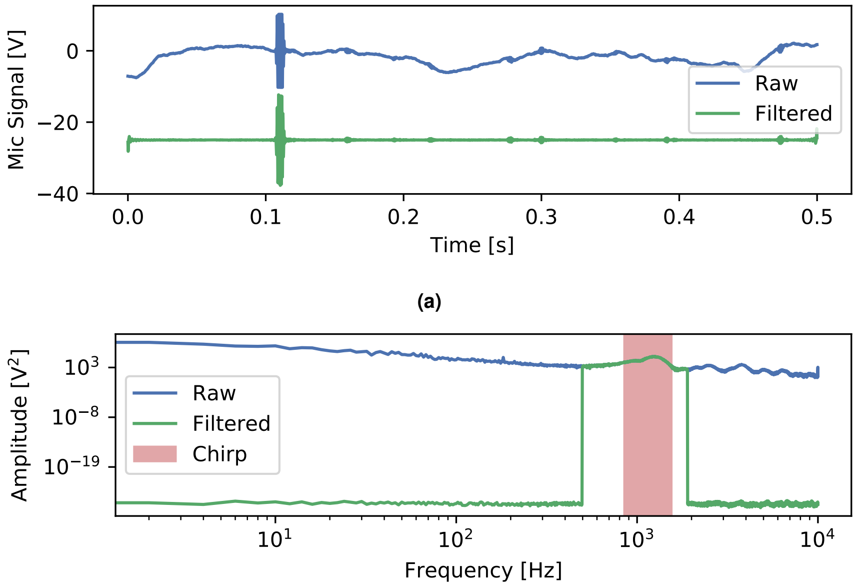

(a)

(b)

Figure 6. Comparison of example microphone data and signal conditioning: (a) raw and filtered microphone time series and (b) frequency spectra of raw and filtered microphone signals.

In addition to acoustic signal frequency filtering, upsampling is employed to refine the travel time estimates. The specified time resolution of the acoustic emissions and recordings is 20 kHz, the accepted upper limit of human perception. Given an average speed of sound of $c = 340$ m/s, this time resolution corresponds to a characteristic spatial resolution of 0.017 m. Alternatively, with a fixed path length r, a sampling rate of 20 kHz leads to an accuracy in path velocity estimation on the order of ± 0.01 m/s. Upsampling the acoustic data increases the precision of the estimated path velocity and acoustic travel time, which in turn reduces the uncertainty in the resultant velocity and temperature field estimates.

3.2.3 Signal Detection

Signal detection to calculate acoustic chirp travel times are identified by cross-correlating received signals with the reference (emitted) chirps. To reduce the computational load, only a small window from each frequency-filtered, upsampled microphone signal is extracted and compared to the reference signal. Only a single reference signal needs to be retained for signal detection because all emitted signals are identical for all speakers and all frames. Figure 7 compares the reference signal (red) to the raw and filtered (blue and green) chirps detected at one microphone. The cross-correlation between the upsampled reference signal and the filtered microphone signal is shown in purple. Red

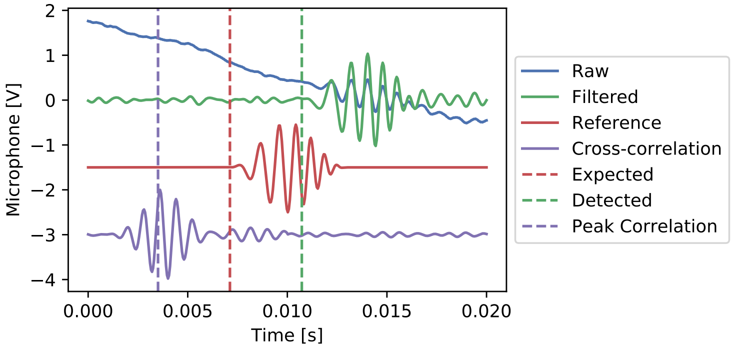

Figure 7. Speaker and microphone signals, emission, and detection times.

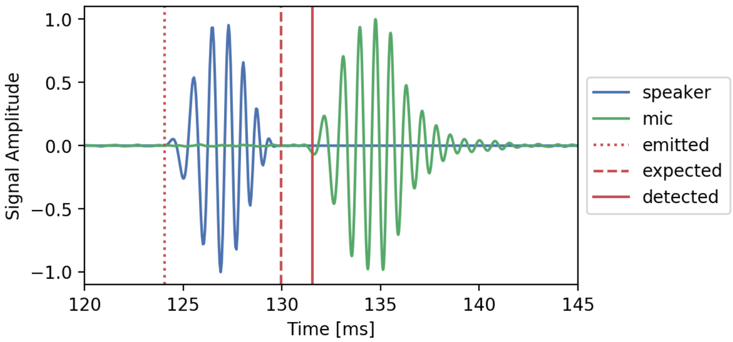

Figure 8. Comparison of emitted, expected, and detected signal times.

and green vertical dashed lines indicate the beginning of the emitted reference signal (t_{emitted}) and the detected signal (t_{detected}) in the microphone data, respectively. The time lag between the vertical red and green lines represents the acoustic travel time $t_{\text{tr}} = t_{\text{detected}} - t_{\text{emitted}}$. The same time lag is identified by the peak value of the cross correlation, shown with the purple vertical dashed line.

Figure 8 shows additional considerations in the detection of acoustic signals. In the figure, the emitted acoustic chirp is indicated in blue and the respective (filtered and upsampled) received signal is shown in green. Red vertical lines indicate the beginning of the acoustic chirp by the speaker (t_{emitted}, dotted), the anticipated speaker reception time by the microphone (t_{expected}, dashed), and the recorded time of the beginning of the chirp at the microphone (t_{detected}, solid). The expected signal arrival time is calculated as

$$t_{\text{expected}} = t_{emitted} + |\boldsymbol{r}_i|/u_i, \tag{3.1}$$

where $\boldsymbol{r}_i$ is the path vector i from a speaker to a microphone, c is the speed of sound estimated by the sonic anemometer, and $\boldsymbol{v}$ is the bulk flow velocity vector estimated by the sonic anemometer. The denominator in Equation (3.1) is the group velocity of an acoustic chirp traveling along path i:

$$u_i = c + \boldsymbol{r}_i \cdot \boldsymbol{v}. \tag{3.2}$$

The difference between the expected signal arrival time and the detected signal travel time is leveraged to estimate the influence of velocity and temperature fluctuations along path i. That difference is labeled as t_i and is used to construct the data vectors used in the TDSI methodology in Equation (2.12). Figure 9 shows plots of filtered microphone signals with expected chirp arrival times.

3.3 System Characterization

The retrieval algorithm for both the bulk velocity and temperature and the fluctuating fields depends on the detected travel times of acoustic chirps across the array. Any signal delay introduced by the hardware or signal processing workflow impacts the estimated flow quantities. To fully characterize the AT array, precise measurements of the

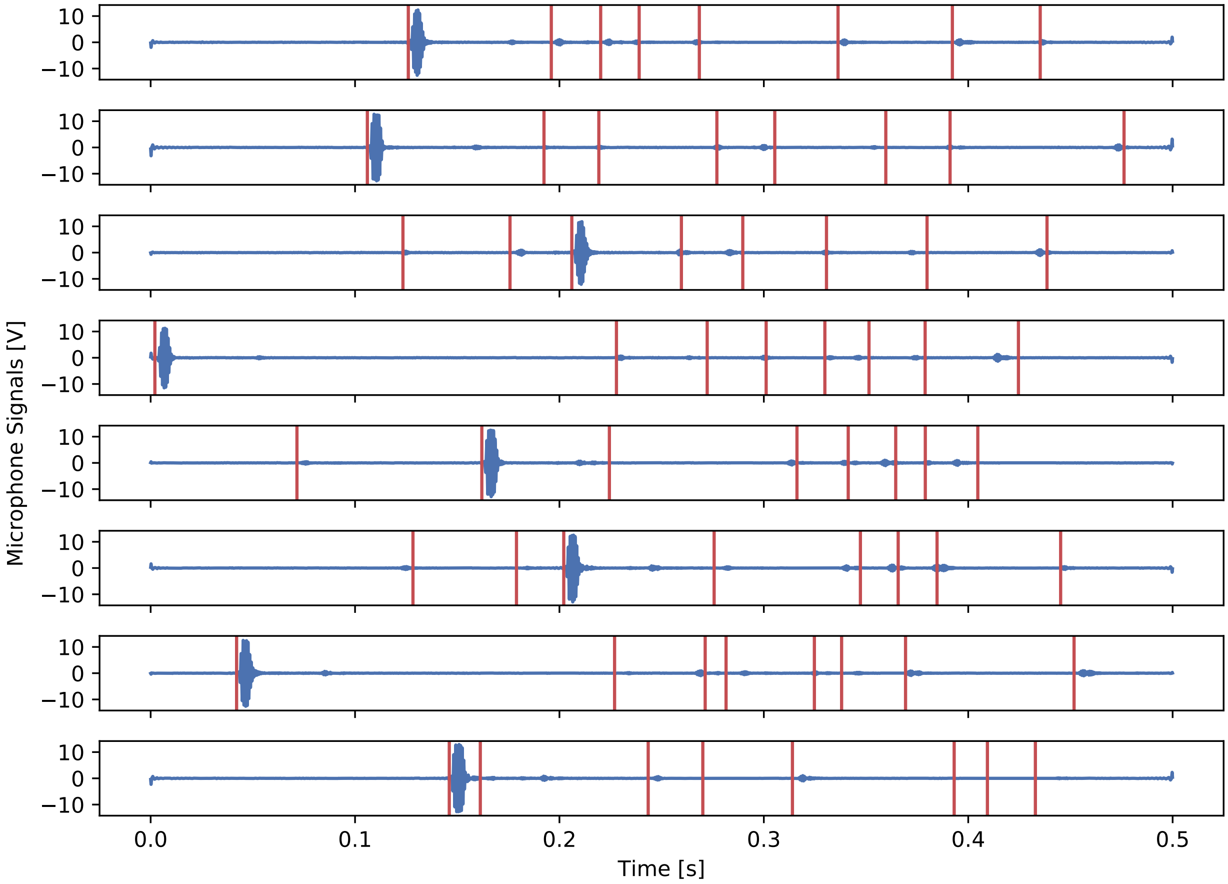

Figure 9. Filtered microphone signals with expected chirp arrival times.

transducer locations in space are needed, as well as estimates of signal latency introduced by the array transducers, and a correction factor that accounts for the non point-source nature of the speakers.

3.3.1 Instrument Location Survey

The first-order requirement for estimation of path velocity and mean flow field and temperature is the location of all acoustic transducers included in the AT array. The precise location information was gathered by repeated survey services. To eliminate uncertainty regarding the location of all speaker aperture centers and microphones, additional surveys were ordered and performed on August 22, 2019. Results from all surveys agree generally, although there are differences reported as large as 0.04 m. Errors of this magnitude in instrumentation locations correspond to an uncertainty in travel time estimates on the order of ±0.001 s. Figure 10 shows the deviations of the most recent instrument location survey to those reported in 2018.

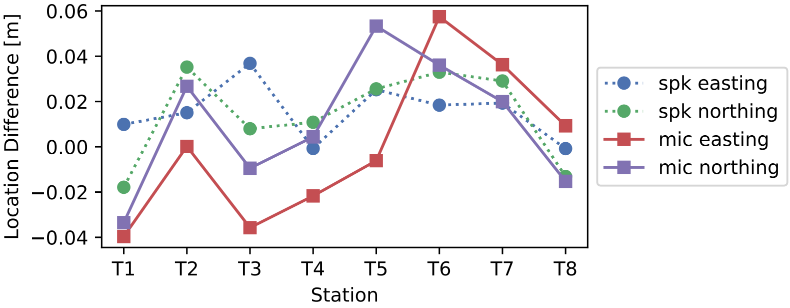

Figure 10. Difference between previously established instrument locations and the average of new survey results.

3.3.2 System Latency Testing

Signal latency associated with each microphone/preamp combination is expected simply because time is required for sensors to actuate, for signals to transmit through the physical system, and for each input to be recognized by the data acquisition system. Given that the resolved flow and temperature fields rely exclusively on very precise estimates of the transit times of acoustic chirps, any delays introduced by the measurement system must be accounted for. Latency testing in the AT array was accomplished by placing one microphone at the aperture of each speaker, producing acoustic chirps, and estimating the delay in signal recognition. Placing the microphone at the aperture of the speaker locates it at the assumed emission point, so the expected travel time should be essentially null.

Figure 11. Microphone affixed to speaker aperture for latency test at Station 8.

Figure 11 shows the test microphone affixed to the speaker at Station 8. The microphone is placed in the center of the aperture and held in place with a bracket affixed to the speaker cone. A coaxial cable (140 m) connects the microphone to the preamp at each station in the array to characterize the latency associated with a chirp emitted from one station and received at another. In each of the 64 speaker/preamp combinations tested (eight speakers and eight preamps), transit times of a total of 120 chirps were recorded.

Because the chirp emission time is specified (i.e., known exactly), a short section of the speaker driver signal centered around the chirp can be extracted. The same time interval was extracted from each of the microphone signals containing the received chirp (Figure 12a).

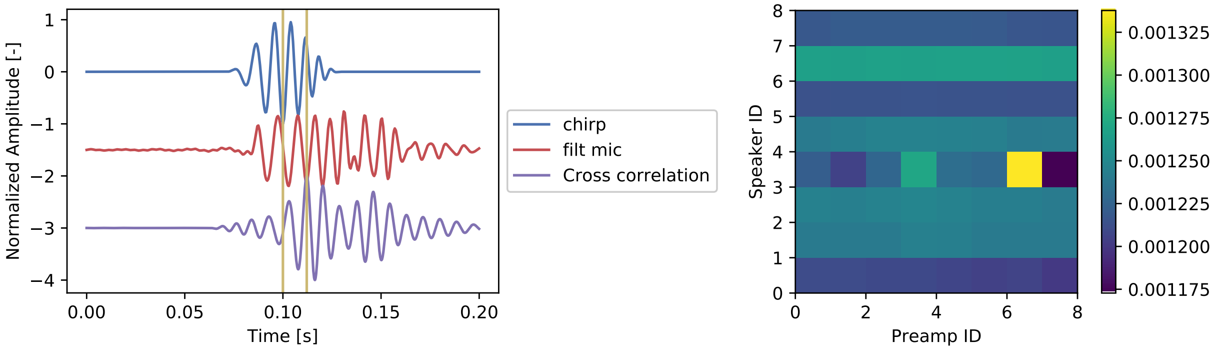

(a) **(b)**

Figure 12. (a) Emitted chirp, filtered microphone signal, and cross correlation. Microphone signal and correlation have been offset vertically. (b) Average signal latency for each speaker/preamp combination.

3.3.3 Speaker Characterization

The theoretical development of acoustic tomography implicitly assumes that sound issues from point sources. In reality, the speakers are not ideal point sources, and distortion is introduced to the chirps as they pass through the cone and out of the aperture. For the purposes of estimating chirp path lengths and transmission times, all acoustic signals are assumed to have sources located in the center of the speaker aperture. However, this assumption requires an additional correction to the delay of signal transmission times.

The sound propagation from the speakers was characterized to map out the variation in travel time from the center of the speaker aperture to various co-planar points located a fixed distance from the center. A test rig was designed to hold a speaker and driver such that the center of the aperture was at a fixed location approximately 1.4 m above ground level. A microphone was supported by a tripod and located at selected radial distances (either 2 m or 4 m) from the aperture center. Acoustic chirps were emitted by the speaker and recorded by the microphone at a range of azimuthal locations around the speaker center, denoted as θ. Figure 13 shows a plane view of the speaker and the coordinate system used for the test. Chirps were emitted every 0.5 s, for a recording period of 1 minute. At each azimuthal location, 120 frames (0.5-s intervals containing a cycle of chirp emission and reception) were recorded.

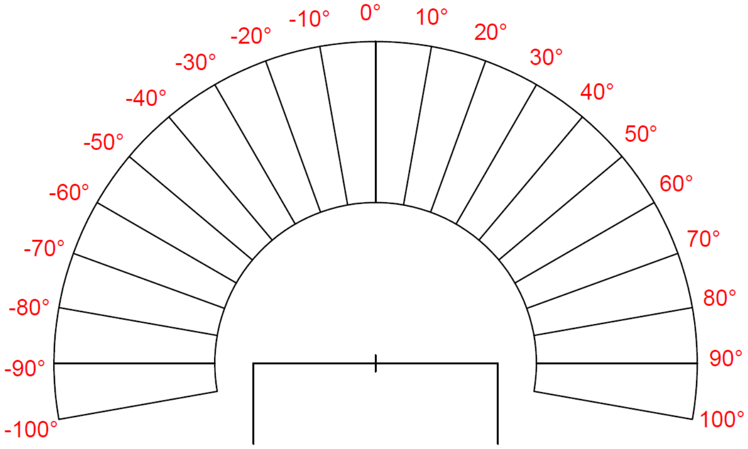

Figure 13. Signal delay test configuration.

The exact time each chirp was emitted from the speaker is specified in the virtual instrument design and is confirmed in the recorded data. With knowledge of the chirp emission time, the distance separating the center of the speaker aperture and the microphone, and the current speed of sound (as recorded by a sonic anemometer on Station 8), the expected acoustic signal reception time can be precisely estimated.

Signal latency, t_{latency}, associated with a particular microphone/preamp combination is the difference between the expected time and the reception time of the acoustic chirp: $t_{\text{latency}} = t_{\text{detected}} - t_{\text{expected}} = t_{\text{detected}} - (t_{emitted} + r/c)$. Travel times for each recorded frame (0.5 s, containing a single chirp) are shown for a few different microphone locations in Figure 14.

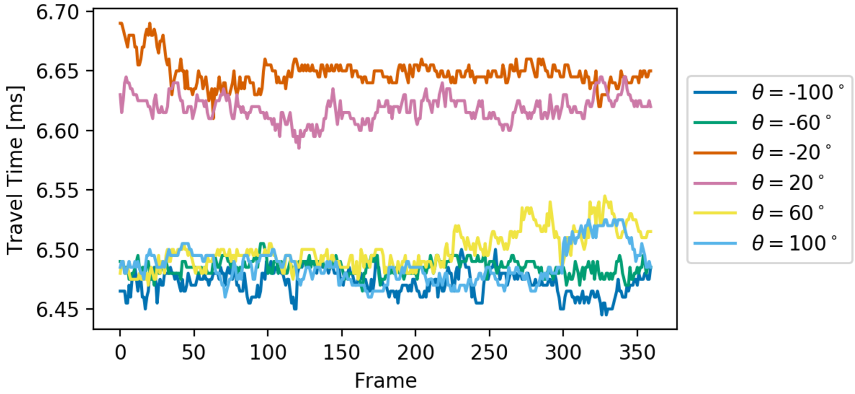

Figure 14. Travel times recorded for each frame depending on azimuthal location of the microphone.

Signal latency introduced by the nonpoint source nature of the speaker is shown in Figure 15. The travel times of detected acoustic signals are shown as blue points and the orange dashed line indicates t_{expected}, for reference. Signal latency varies with the azimuth angle between the speaker's central axis and the microphone location. The vertical offsets in Figure 15 indicate that the B&K microphones introduce latency to the signal recordings on the order of $\sim$ 6.45 milliseconds (ms).

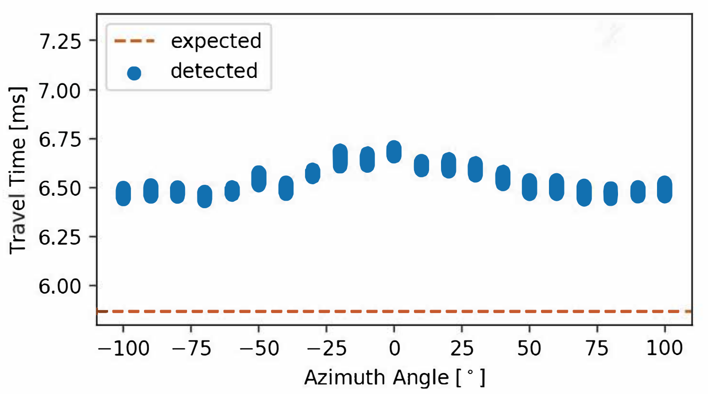

Figure 15. Detection and expected signal arrival times by azimuth angle.

The difference between the detected and expected travel times shown in Figure 15 arises from the nonpoint source nature of the speaker as an acoustic source. Two radial distances, $r = 2$ m and $r = 4$ m, were tested for two candidate microphones considered for the AT array. Figure 16 shows each set of calibration data normalized by subtracting the minimum travel time in order to isolate the difference in travel times with respect to azimuth angle. Solid lines connect the mean time delay for the microphone for use in the AT array at each azimuthal position; error bars indicate the respective standard deviation. Data from prior calibration tests are shown in purple (for $r = 2$ m) and yellow (for $r = 4$ m), verifying that the nonpoint source characteristics of the speakers are consistent over multiple tests. The trend lines for previous data show a sinusoidal function modeling the data using a least-squares fit according to

$$t_{\text{fit}} = a * \cos(b * \theta) + c, \tag{3.3}$$

where θ is the azimuth angle and a, b, and c are the model fit parameters.

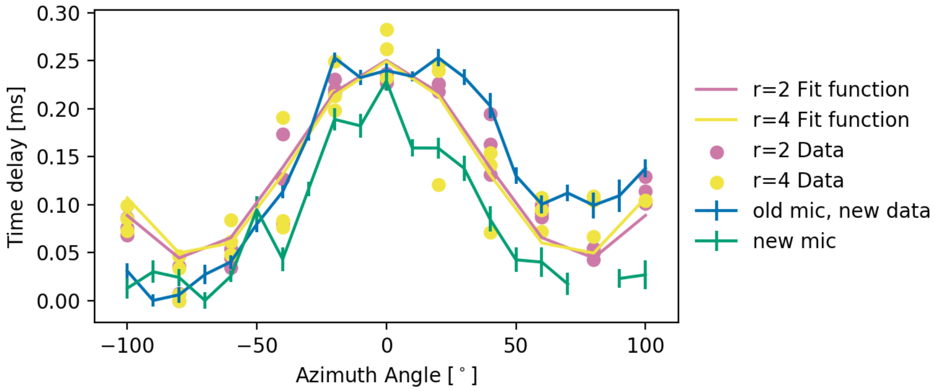

Figure 16. Absolute range of differences in signal travel times. Purple and yellow are previous results; blue and green are results of the recent test.

Fitting parameters for speaker characterization tests are presented in Table 2. The coefficient of determination (R^2) value for each curve indicates a moderately good fit between data and fit function. The fit does not take into account any skew or asymmetry evident in the data; neither has any outlier detection and elimination been undertaken.

Table 2. Fit parameters and coefficients of determination for speaker characterization tests

	a	b	c	R^2
$r = 2$ m	0.104	2.36	0.147	0.892
$r = 4$ m	0.102	2.47	0.147	0.828

3.3.4 Self-Calibration

Taking the calibration information from instrument locations, signal latency, and nonpoint source emission into account, the expected travel time of acoustic chirps can be precisely estimated. As a final step to eliminate uncertainty in the travel time of acoustic chirps, a two-step "self-calibration" was performed for the array. Data for self-calibration of the AT array were collected in quiescent conditions, where the ambient flow was minimal and the 2.1 kW wind turbine (XZERES Wind Skystream 3.7) within the AT array was not functioning. With the rotor parked, the turbine created a small, bluff-body wake, rather than a large momentum deficit corresponding to the energy extracted from the atmosphere.

The first step in self-calibration involves removing any remaining systematic bias in travel time estimates from the recorded data. Remaining uncertainty in calibration of the AT array (beyond instrument locations, signal latency, nonpoint source emission, and sonic anemometer orientation angle) is quantified by comparing the expected travel times during quiescent conditions to the estimates reported via signal detection by the array. During quiescent conditions, the ambient flow speed is small (< 2 m/s), and the group velocity, u_i, along every path, r_i, reduces to the speed of sound, c, alone. Considering this, the observed travel times, t_i, along all transmission paths, r_i, should closely match the value expected, t_{expected}, as the ratio of path length and local speed of sound:

$$t_{\text{expected}} = |\boldsymbol{r}_i|/c. \tag{3.4}$$

Figure 17 shows the observed travel times, t_{observed}, along selected paths throughout the self-calibration data collection period. Paths are colored according to the paths indicated in Figure 4. The bottom chart features the same observed travel times subjected to a rolling average of 10 frames (5 s) for clarity.

In reality, the atmosphere was not perfectly quiescent during the self-calibration data collection period, and the atmospheric flow is still taken into account, although it remained less than 2.0 m/s, and the Skystream 3.7 remained parked. The expected travel time can then be estimated following Equation (3.4) and compared to observed travel times. Figure 18a shows the mean travel time for acoustic chirps along each of the travel paths, $\overline{t_i}$. Figure 18b indicates the remaining latency ($t_{\text{latency}} = t_{\text{observed}} - t_{\text{expected}}$) averaged over the 1,200 observations (10 min. of data,

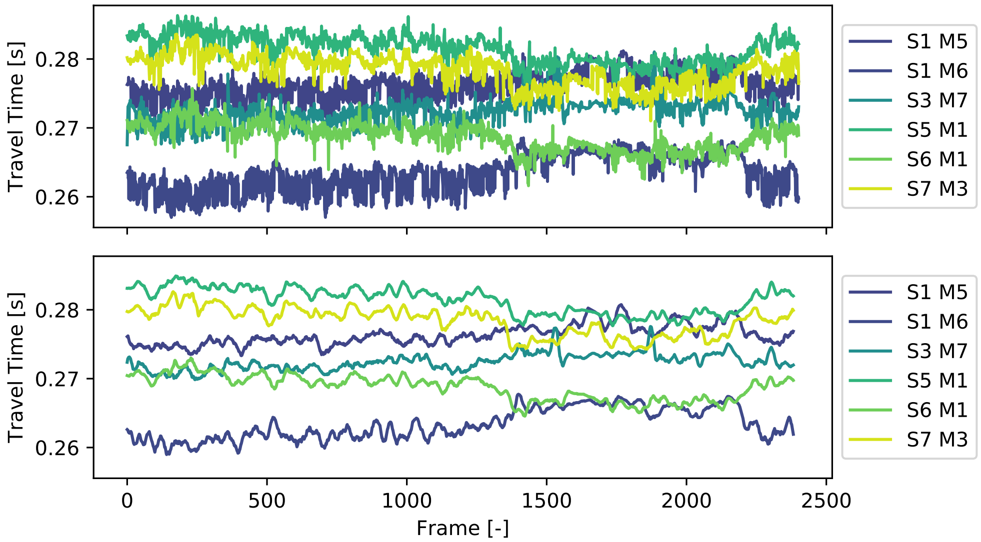

Figure 17. Comparison of observed travel times for selected paths over 20 min. of self-calibration data collected in August 2019.

velocity estimates provided by the AT array at 2 Hz). The solid line in Figure 18b indicates the average latency, $\bar{t}_{\text{latency}}$, and the shaded region indicates the standard deviation of t_{latency} for each path.

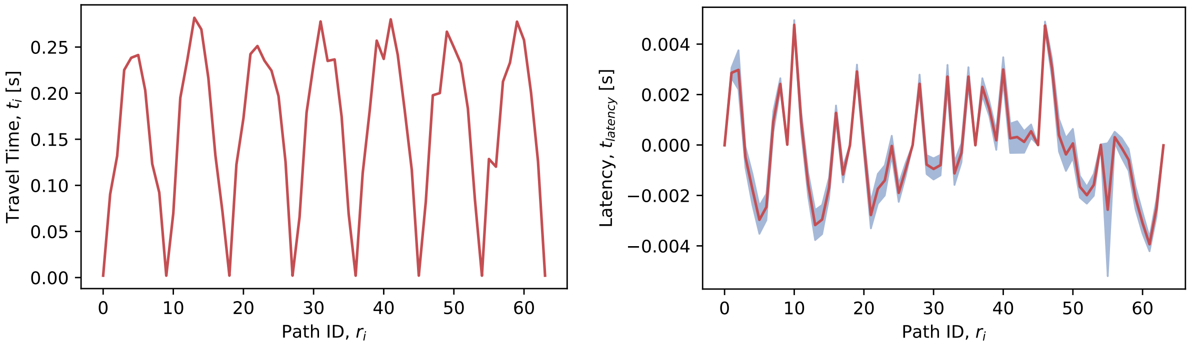

(a) **(b)**

Figure 18. Self-calibration of travel times: (a) average travel time $\bar{t}_i$ along each path r_i and (b) average and standard deviation of t_{latency} for each path.

The second step of the self-calibration process minimizes root-mean-square error (ε) between the reported 2D velocity vectors from the array and the sonic anemometer, $\boldsymbol{u}_0$ and $\boldsymbol{u_s}$, respectively. Error is calculated as

$$\varepsilon = |\boldsymbol{u}_0 - \boldsymbol{u}_s|, \tag{3.5}$$

where the vertical lines denote a vector norm. Because the group velocity $\boldsymbol{u}_i$ depends on the projection of the ambient flow velocity vector onto each path vector, changing the assumed orientation angle of the sonic anemometer can have a large and nonlinear impact on the estimated group velocity. Therefore, this also impacts the anticipated arrival times of acoustic chirps and the estimate of the bulk flow vector by the AT array.

The sonic anemometer reports each of the vector components of velocity (u_s, v_s, and w_s) at 20 Hz with a default coordinate system relative to the geometry of the structure of the anemometer. In the AT array, the sonic anemometer is not aligned to 270°, which would report u_s and v_s aligned to east-west and north-south flow according to the conventional Cartesian coordinates. Instead, the orientation of the sonic anemometer, θ, must be taken into account to correctly estimate the contribution of u_s and v_s to the Cartesian components of velocity in the AT array according to

$$[u, v] = \boldsymbol{R} \cdot [u_s, v_s], \tag{3.6}$$

where $\boldsymbol{R}$ is a rotation matrix using the sonic anemometer orientation angle:

$$\boldsymbol{R} = \begin{bmatrix} \cos\theta & \sin\theta \\ -\sin\theta & \cos\theta \end{bmatrix} \tag{3.7}$$

Figure 19 shows ε for 10 minutes of data collected during calm atmospheric conditions on August 6, 2019. Each of the light blue lines indicates the ε of 1 minute of data, while the bold blue line indicates the average error as a function of orientation angle, θ. Minimum average ε is achieved for a sonic anemometer orientation angle of $\theta = 8.2°$, indicated by the dashed green vertical line.

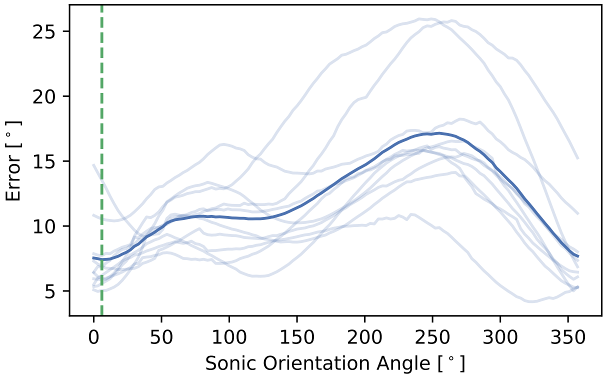

Figure 19. Root-mean-square error (ε) between $\boldsymbol{u}_0$ and $\boldsymbol{u}_s$ by orientation angle θ.

The maximum combined signal latency from the nonpoint source nature of the speakers, the signal transmission delays in the array hardware, and latency from the self calibration is on the order of 0.01 s. Signal transmission times in a quiescent atmosphere (Figure18) are between 0.1 s and 0.28 s. The maximum combined signal latency represents a systematic error in measured travel time between 3.5% and 10%. During non-quiescent measurement periods, when the bulk velocity is greater than 2 m/s, additional error is expected as the assumption that the bulk flow velocity within the array is the same as that of the sonic anemometer becomes more uncertain.

3.4 System Limitations

Several key assumptions underpin the retrieval method used by the AT system. These assumptions impact the application of the system for R&D in the renewable energy space. Among other things, the TDSI method (Section 2.2) assumes that fluctuations of velocity and temperature are normally distributed, independent of bulk flow quantities, statistically stationary, and spatially homogeneous. These are strong assumptions in the ABL, especially at the Flatirons Campus. Although these assumptions simplify the inverse problem, they also act to limit the validity of the method for wind turbine wakes and other flows with strong mean shear graidents.

Perhaps the single greatest limiting factor is the assumption that the velocity and temperature fields fluctuate around a homogeneous background flow. This assumption conditions the inverse problem to ignore any persistent mean shear gradients or spatial variability typical of wakes and other industrial flows. Theoretical development by the NREL research team relaxes this constraint by considering a nonhomogeneous background flow in both the forward and inverse problems. Results from this research area are expected in Fiscal Year 2023, and will be shared at the 24th Symposium on Boundary Layers and Turbulence, organized by the American Meteorological Society in Denver, Colorado, in January 2023 (Maric and Hamilton 2023).

The second assumption being assessed by the NREL research team is that of normally distributed fluctuations. The classic TDSI method developed by Ostashev et al. (2009) assumes a constant length scale (l) for both velocity and temperature fluctuations, which in turn acts as the limit of spatial resolution. Although the overdetermined problem can provide measurement points at a resolution of approximately 1.25 m, the method can only resolve structures with length scales greater than l. This assumption can be tested numerically against the reference data recorded by the sonic anemometer. Adding a multiscale covariance model to the TDSI problem will address the resolution limit introduced by the assumption of a fixed and constant fluctuation length scale. The NREL research team will test multiple multiscale covariance models with the intent of implementing the least computationally intensive model producing the closest results to point measurements.

3.5 Validation Objectives

Acceptance of AT into the range of observational capabilities for turbulent flows in the atmosphere requires that measurements be carefully vetted for possible sources of uncertainty and error. Error quantification requires post hoc comparison of flow and temperature fields as well as a detailed analysis of uncertainties. These uncertainties arise from the theoretical formulation underlying AT and the particular equipment and signal processing methods employed in field estimation. Comparison of the resolved flow and temperature fields to in situ point measurements, and alternate remote sensing methods will help to establish the capabilities of AT for applications by the atmospheric and wind energy research communities.

Comparison to previous AT work. The capabilities of the prototype array will be evaluated to ensure that the AT array is able to reproduce the performance seen in past studies. A complete review of the theoretical basis for fluctuating temperature and velocity field reconstruction will be undertaken specifically to determine the most promising methods for the intended applications of the technology. Measurement capability of the AT system will be quantified for a range of atmospheric stability conditions.

Comparison to point measurements. A sonic anemometer (Campbell Scientific CSAT3) and temperature/humidity probe (Vaisala HMT337) have been added to one of the towers in the prototype AT array at NREL. Velocity and temperature estimates from the AT system deviate from those provided by the sonic anemometer due to the difference in location of the estimated bulk (spatially averaged) atmospheric quantities and the point measurements at the edge of the array. Outfitting the AT array with additional sensors will provide validation data at more locations bordering and within the AT interrogation area.

Validation against lidar observations. Establishing AT as a viable remote sensing method requires direct comparison to existing remote sensing technology under tightly controlled conditions. Profiling and scanning lidars and in situ instrumentation will be employed to characterize the heterogeneous flow across the array, including regions outside the AT array, as the atmospheric flow outside the interrogation area will affect the flow structures within the AT array. Detailed comparison of the various remote sensing and point measurement methods for atmospheric flows and observation of the wake from a subscale wind turbine will highlight capabilities of the proposed technology and identify sources of error and uncertainty. Measurement with multiple technologies will provide strategies and methods for leveraging advantages of multiple instruments for a more complete view of the atmosphere for future field campaigns.

In situ calibration method. Robust operation of the AT array for atmospheric observations requires a reliable calibration methodology that accounts for any uncertainties in the emission and detection of acoustic signals. Additionally, verification of the sensors and signal processing methods as well as validation against redundant instrumentation is required. Any sensitivity of the system to operating conditions that lead to signal delay for transmission or detection will reduce the accuracy of the resolved velocity and temperature fields. An in situ calibration method will track latency in signal propagation through the AT array hardware, data acquisition system, deviation from point-source acoustic propagation models, and acoustic reflection off of solid surfaces. Calibration offsets for signal latency will be tracked over time and will provide insight to the overall health of the array.

4 Results

Precisely calculating the travel time between each source/receiver pair yields a series of travel times, shown for selected travel paths in Figure 20. The color of each time series reflects the corresponding travel path shown in Figure 4. Considering the series of acoustic travel times for each chirp, the bulk velocity and temperature are estimated according to Equation (2.8).

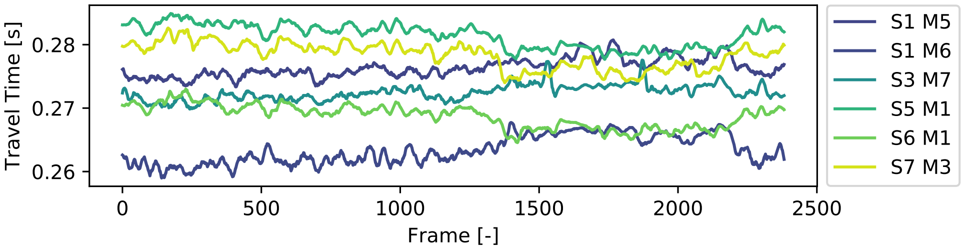

Figure 20. Calculated travel times for selected speaker/microphone pairs.

Figure 21 compares bulk estimates of in-plane components of velocity and temperature to observations collected with a sonic anemometer located at the corner of the array during a period of nearly quiescent conditions at the Flatirons Campus. Deviations seen between the AT and sonic anemometer signal arise from the spatial averaging of the bulk flow due to the inverse calculations within the AT method. The series of observed travel times are then used to estimate the spatially heterogeneous fields of velocity and temperature, shown in Figure 22.

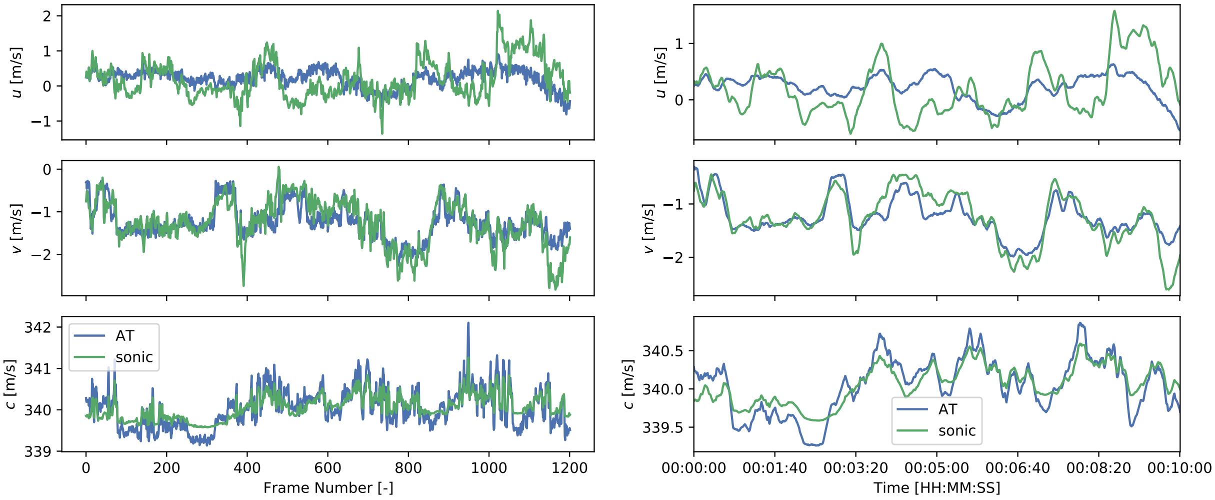

(a) **(b)**

Figure 21. Spatial average values of velocity components and speed of sound during self-calibration data: (a) flow velocity component and speed of sound comparison between AT array and sonic anemometer; (b) rolling average of velocity and speed of sound estimates from the AT array and sonic anemometer.

The AT array was tuned by quantifying known sources of latency throughout the system and executing the self-calibration procedure to eliminate systematic biases in travel time estimation and in the sonic anemometer orientation angle, θ. As a result, the mean bulk velocity estimates from the AT array closely match the velocity reported by the sonic anemometer. Figure 21 compares the east-west components of velocity (top), the north-south components of velocity (middle), and the estimated speed of sound (bottom) for the calibration data. The remaining disagreement between the sonic anemometer and the AT array arises from the source and nature of the velocity estimates. Sonic anemometers report high-frequency velocity estimates at one point, in this case located at the corner of the array. The AT array estimate of the velocity vector reconciles the travel time of many acoustic chirps over a very large range, providing a spatially averaged estimate.

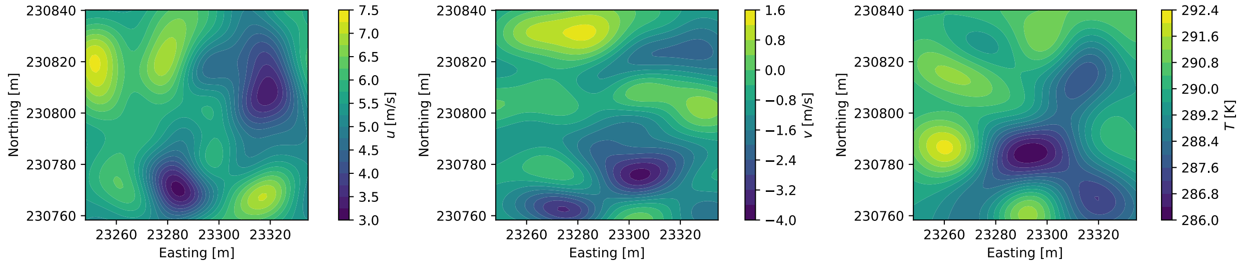

Figure 22. Reconstructed snapshot of u, v, and T from the prototype array at a resolution of 1.25 m $\times$ 1.25 m.

Figure 23 compares mean field data from the AT array to that of the sonic anemometer for a period of data collection on August 15, 2019. During the data collection period, winds were moderate and originated from the prevailing wind direction around 285°. Data were collected for a total of 20 minutes, leading to 2,400 frames of data for which spatial average data and fluctuations could be estimated. As with the calibration data above, Figure 23 shows the east-west and north-south components of velocity on top, followed by the estimated speed of sound within the interrogation area. On the left are mean field estimates at the full resolution of 2 Hz, and on the right are the same data subjected to a rolling average of 5 s. Mean speed of sound and east-west velocity (c_0 and u_0) estimated by the AT array agree well throughout the recorded data. The north-south component of velocity (v_0) shows a considerable difference from the sonic anemometer in the second 10-minute segment of data. During that time, the sonic anemometer reported a larger magnitude to the south than the AT array. These differences likely reflect influence of the data shed located to the north in the local estimated velocity from the sonic anemometer. Table 3 compares the averages of estimated velocity and temperature of the AT array and the sonic anemometer.

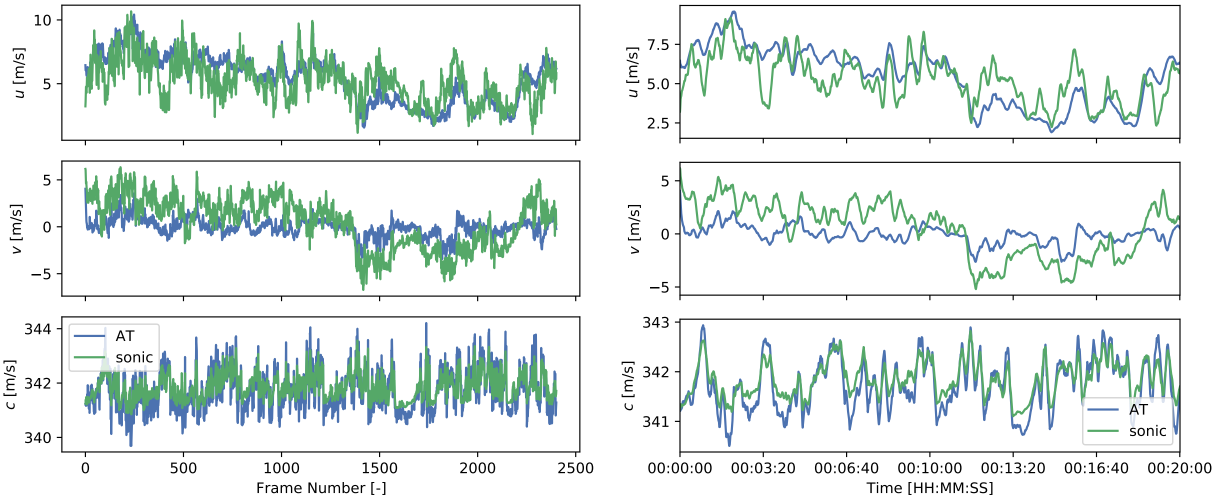

(a) **(b)**

Figure 23. Spatial average values of velocity components and speed of sound for data from prevailing wind direction: (a) flow velocity component and speed of sound comparison between AT array and sonic anemometer; (b) rolling average of velocity and speed of sound estimates from the AT array and sonic anemometer.

Table 3. Comparison of temporally and spatially averaged temperature and velocity fields

Mean Fields	u_0 [m/s]	v_0 [m/s]	c_0 [m/s]
Sonic Anemometer	4.46	-2.80	341.85
AT Array	4.91	-1.48	341.65

Figures 24 and 25 compare examples of field reconstructions of the in-plane components of velocity and temperature following the TDSI algorithm outlined in Section 2. Although no direct observations are available, or even possible with other technologies, against which quantitative comparisons may be made, the TDSI algorithm does provide a thorough uncertainty quantification method.

Following the methods outlined in Vecherin et al. (2006), uncertainty in the field reconstructions may be estimated directly as the L_2-norm of the difference between the model and the data covariance matrices (see Equation (2.18)). Normalized mean square error (NMSE) indicates the variance between model and data covariance matrices, normalized by the respective field variances. An NMSE of order unity indicates that the errors of reconstruction are of the order of the variance of the original field (i.e., one has a poor reconstruction). Conversely, if NMSE of any given reconstruction is zero, it is expected that the reconstructed and actual fields are identical. NMSE can be recalculated into root-mean-square errors, or more specifically, the standard deviations (STD) between model and data covariances.

Reconstructed fields are shown for u (Figure 24a) and v (Figure 24b), followed by their respective NMSE (Figure 24c and 24d) and STD (Figure 24e and 24f) fields. Similarly, the reconstructed temperature, T, is shown in Figure 25a, followed by fields of NMSE(T) and STD(T) (Figure 25b and 25c). Note that these figures are reconstructions of the velocity and temperature fields during a single frame and represent the fluctuating flow during one 0.5-s period. Table 4 shows the reconstruction errors associated with each of the fields featured in Figures 24 and 25.

Table 4. Error associated with covariances of reconstructed fields of temperature and velocity

Fields	u		v		T	
Errors	NMSE	STD [m/s]	NMSE	STD [m/s]	NMSE	STD [K]
	0.5430	0.0319	0.5010	0.0445	0.3720	0.0319

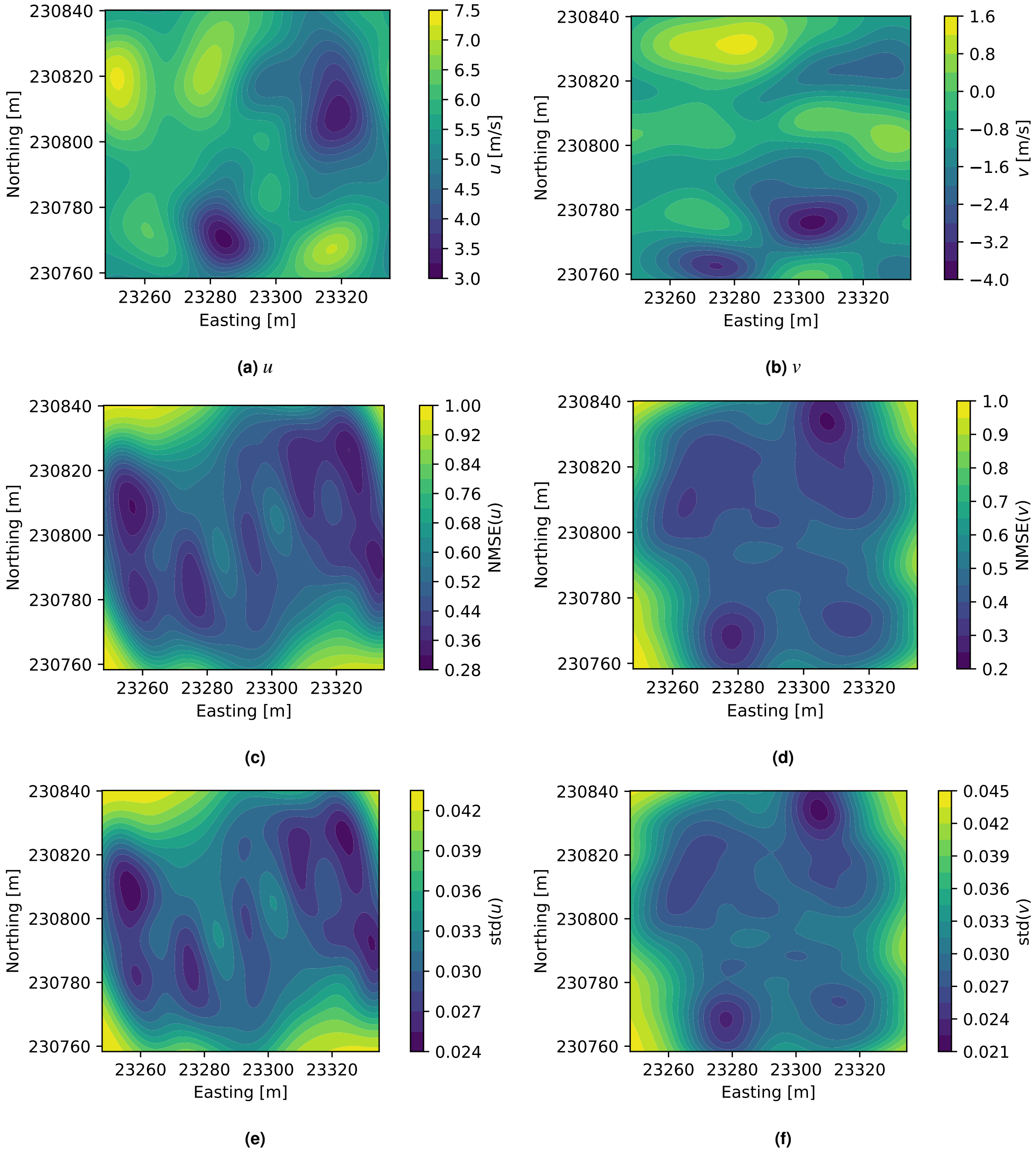

(a) *u*

(b) *v*

(c)

(d)

(e)

(f)

Figure 24. In-plane velocity components of (a) u and (b) v as well as the normalized mean-square error associated with retrievals (c) NMSE(u) and (d) NMSE(v), and the standard deviations of each velocity component (e) STD(u) and (f) STD(v).

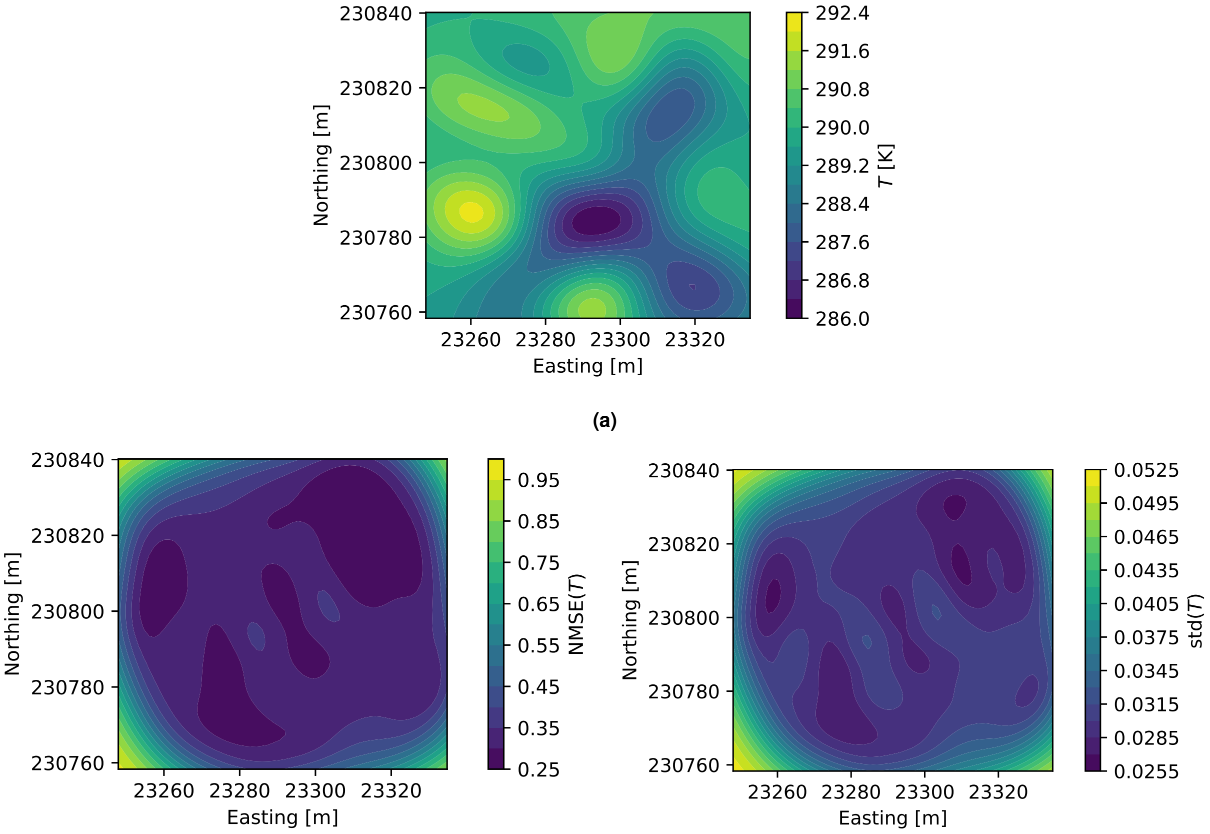

(a)

(b)

(c)

Figure 25. Temperature field (a) T, (b) NMSE(T), (c) STD(T).

5 Future AT Array Configurations and Capabilities

5.1 3D Array

The planar configuration of the AT array is sufficient for a proof-of-concept development of the method; atmospheric turbulence and wind energy flows are inherently three-dimensional (3D). Development of the AT array to be able to interrogate and resolve 3D flows requires significant hardware and software considerations to be able to efficiently observe 3D turbulent flow and temperature fields. Augmenting the array with additional acoustic transducers will increase the acoustic travel paths considered in field reconstruction and will extend the interrogation area to a 3D volume. Additional transducers will further increase the spatial resolution of the AT array but will come at the cost of additional signal processing load. A simple illustration of what a 3D array at NREL would look like is shown in Figure 26. The 3D AT system will be able to observe velocities and temperatures as volumetric snapshots. These capabilities will lead to improved understanding of atmospheric science. To date, 3D acoustic tomography has only been implemented on 6-m masts; the AT array at the National Renewable Energy Laboratory's (NREL's) Flatirons Campus is already equipped with 10-m towers. The first research application of the AT array at NREL will be to characterize the fluctuating velocity and temperature fields of the atmospheric boundary layer (ABL) over locally flat terrain, subject to regional flow effects from the nearby Rocky Mountains and other geographical influences. Fundamental atmospheric research with the AT system will result in new insights regarding local-scale spatial variations in shear stresses, the friction velocity, and turbulent heat flux between the ground and ABL. Coherent structures near the surface carry most of the turbulent kinetic energy in the ABL and remain difficult to effectively characterize. The development of the AT array will lead to unprecedented and invaluable information, yielding advancements in the understanding of fundamental atmospheric processes.

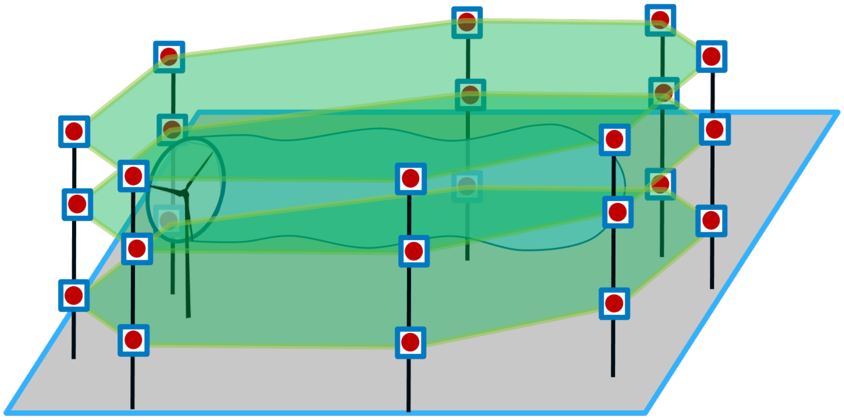

Figure 26. 3D AT array adding two levels to the existing hardware and developing the capability to resolve vertical gradients, heat, and momentum flux.

5.1.1 Additional Capabilities

Adding additional acoustic transducers to the existing AT array at Site 1E will allow the NREL research team to focus on measurements that include a vertical component. A common assumption in atmospheric science and wind energy research is that there is no mean vertical component of velocity. While this assumption is consistent in a time-averaged sense, turbulent motions, variances, and topography-driven vertical flows are not expected to be two-dimensional. The flux of scalar quantities, including momentum, kinetic energy, heat, and moisture, are all important to wind plant flow dynamics and local climatology studies and are within reach of a 3D AT array system. A 3D system is more effective in the characterization of turbulence and coherent structures and the study of temperature and velocity eddies. Furthermore, it will provide a means to obtain near-ground heat and momentum fluxes for validation of large-eddy simulation (LES) models as well as account for atmospheric stratification. Stratification also plays a large role in sound propagation in the ABL as it leads to the refraction of sound (Ostashev and Wilson 2015).

5.1.2 Required Upgrades

Upgrading the AT array system to interrogate a 3D volume with acoustic signals involves adding two additional transducer sets (speaker and microphone) to each of the support towers forming the array. While NREL already owns speakers and drivers to accommodate the expanded set of transducers, additional microphones and data acquisition hardware will be necessary to complete the system expansion. The NREL research team will source microphones of identical make, model, and capability to those already in place to simplify integration into the data acquisition system.

5.1.3 Applications

The 3D AT array has immediate applications in the renewable energy technology R&D space as well as in fundamental atmospheric science studies. The Skystream 3.7 wind turbine in the array is free to use for method development, uncertainty estimates, and quantification of limits in accuracy and resolution. Adding two additional layers of transducers to the acoustic array will increase the spatial and temporal resolution of the system and increase the fidelity of the field retrieval to measure fluctuating velocity and temperature. TDSI, the retrieval method currently used in the AT processing software, reconstructs fluctuating fields based on specified covariance relationships around a homogeneous background flow. Resolving a wind turbine wake requires updates to the TDSI process to include both a nonhomogeneous background flow (e.g., estimated online with the FLOw Redirection and Induction in Steady State (FLORIS) simulation software) and eventually an adaptive turbulent fluctuation covariance scheme that accommodates local shear gradients from the wake.

By generalizing the algorithm to accommodate nonhomogeneous flows that are not necessarily prescribed ahead of time, the system should be able to resolve mean flow gradients introduced by any sort of structure. Concentrated solar power installations (parabolic troughs and heliostats), building or vehicle wakes, and complex terrain-induced flows are all within reach of the measurements made by the AT system with a suitably generalized retrieval algorithm.

High-resolution 3D snapshots of the atmospheric surface layer represent a significant step forward in measurement technology—no other technologies exist for collecting similar observations. Accordingly, measurements made in the 3D AT array are immediately beneficial to fundamental atmospheric science research as well as renewable energy applications. The 3D AT array should be able to resolve velocity and temperature fields associated with individual turbulent structures within the interrogation area, allowing researchers to characterize the heat and momentum flux associated with particular structures and heterogeneity of transport mechanisms within the array.

5.2 Utility-Scale System

Applying the AT technology to utility-scale turbines will require a significant scaling effort, but will provide the immediate reward of characterizing turbulent flow features incident on a wind turbine rotor and in the near wake. The most straightforward approach to applying AT at the utility scale will be to arrange transducers bordering a vertically oriented interrogation area (Figure 27) that includes at least a part of the rotor. While this configuration will provide measurements analogous to the existing 2D array, and thus will not provide 3D snapshots of the turbulent flow, the system will be able to measure a slice of the flow that includes the induction zone and rotor-added turbulence.

No equivalent measurement system exists—scanning lidar is the closest alternative, but can provide only line-of-sight data along a beam that must sweep an area of interest and cannot produce reliable measurements near solid bodies. Additionally, scanning lidars must balance scan rate, accuracy, and resolution. Assuming acoustic transducers can be arranged on a set of two towers spanning the rotor height of a utility scale turbine with an 80 m diameter, the utility-scale AT array should be able to provide nearly uniform snapshots of temperature and velocity with a resolution on the order of 5–10 m every 3–3.5 s. Additional development on acoustic signal design to assign each chirp a unique form (central frequency, bandwidth, duration) will increase the temporal resolution of the system by at least a factor of 2, to 1.5 s. Giving each signal a unique design over three to five frames would increase the resolution by another factor of 2 to 4, to a final temporal resolution of approximately 0.5 s. Every increase in temporal resolution through acoustic signal design will increase the complexity and computational load of the signal processing effort.

The current design idea for a utility-scale AT system consists of supporting transducers arrayed vertically along two towers. The sketch in Figure 27 shows two towers holding five transducer locations each, for a total of 100 travel paths, 90 omitting co-located transducers. Further omitting travel paths connecting sensors on the same tower would further decrease the travel paths to 50.

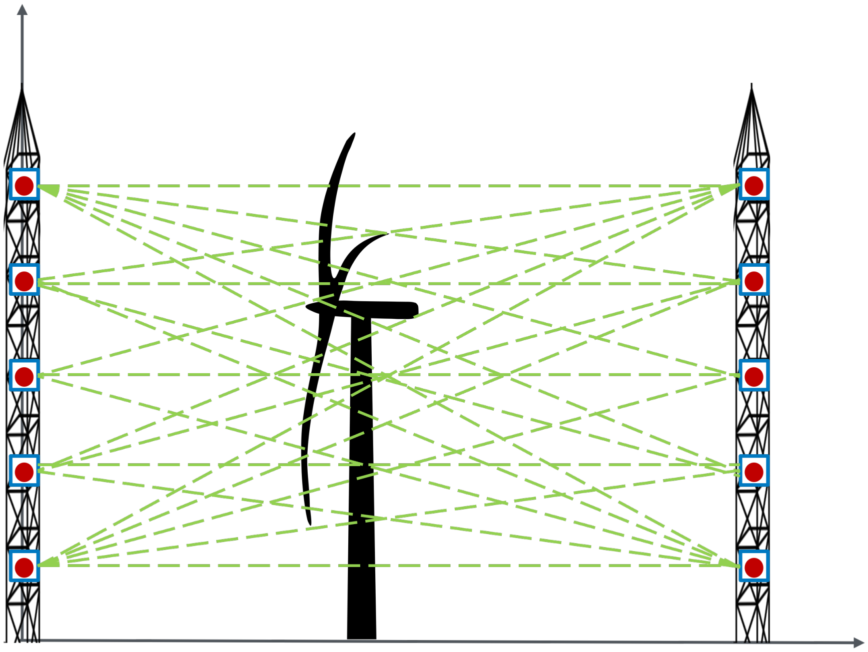

Figure 27. AT array supported on tall towers surrounding a utility-scale turbine.

5.2.1 Equipment

The most obvious target for developing a utility-scale AT system described here would be at the Flatirons Campus, which already houses multiple meteorological (met) masts capable of supporting speakers and microphones. The M5 met mast directly upstream of the DOE-owned GE 1.5-MW turbine has already been used to host acoustic sensors for studies of vertical signal propagation through inhomogeneous media (Kamrath et al. 2021). See Figure 28. This mast can be outfitted again with acoustic sensors and data acquisition systems with only a moderate effort from NREL researchers. To complete the utility-scale AT array, a second tower is needed for which there are two options.

Figure 28. M5 met mast at the NREL Flatirons Campus showing a microphone and meteorological boom from the Kamrath et al. (2021) study.

The ideal setup would be to place a second tower downstream of the GE 1.5-MW wind turbine at the Flatirons Campus in order to align a vertical plane with the prevailing wind direction and include the rotor or hub of the turbine. Locating a tower two rotor diameters downstream of the GE 1.5-MW wind turbine, however, would place it on the Rocky Flats National Wildlife Refuge, which may present a regulatory or administrative challenge.

As an alternative, one of the other existing towers on the Flatirons Campus could host the complement of acoustic sensors needed to complete the utility-scale AT array. A smaller tower (M3, 100 m) is located roughly 250 m to the southwest of M5 and could act as an additional structure to host acoustic transducers, forming a vertical plane as an interrogation area (Figure 29). Using M3 and M5 to form the array would limit the maximum vertical span of the array to that of the shorter tower and would not be able to cover the full 135-m height of the rotor of the GE 1.5-MW wind turbine. The interrogation area would not span the rotor or the induction zone of the GE 1.5-MW wind turbine, but could include a part of the wake region for certain wind directions and provide validation of the method for utility-scale turbines.

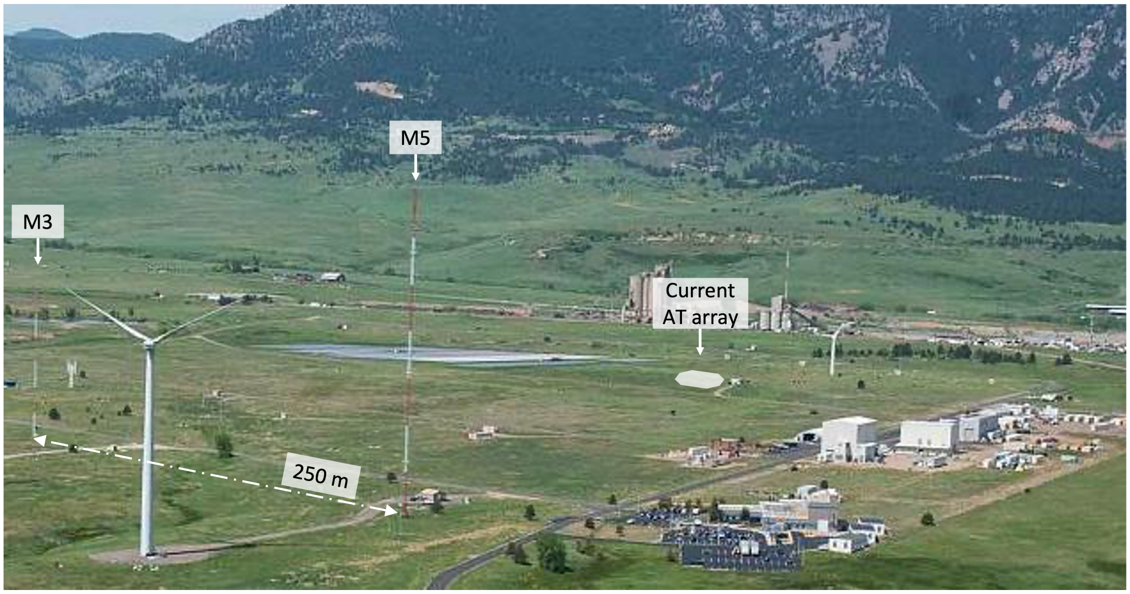

Figure 29. NREL Flatirons Campus, highlighting the M5 met tower to the west of the GE 1.5-MW wind turbine and the M3 tower 250 m to the south.

In building the utility-scale AT array as a follow-on project to the 3D AT array described in Section 5.1, much of the suite of sensors and equipment can be used to instrument towers—no additional speakers, drivers, or microphones will need to be acquired to outfit the utility-scale AT system. The utility-scale system will require investment in terms of materials (cabling, support mechanisms, etc.) and data acquisition hardware.

5.2.2 Engineering Challenges

The span of the utility-scale AT array system is similar to that of the existing AT array, resulting in no significant differences in signal attenuation by the atmosphere. Reflection of acoustic signals off of the ground and the blade and tower structures of the turbine itself may complicate signal identification and processing. The NREL research team, however, already has a processing strategy in place to minimize erroneous signal identification in the retrieval process.

Signal transit time across the increased scale will be a limiting factor in the temporal resolution of the system to 3–3.5 s, although updating and varying the signal design should increase resolution by a factor of 2 to 8, noted above. Without changing the acoustic signal design, observations will represent a flow field integrated over the temporal resolution of 3–3.5 s. Temporal resolution of the AT array and the representation of short-time-scale turbulence will be a priority for the NREL research team. The spatial resolution of the system will be limited by the number of ray paths crossing the interrogation area (indicated with green dashed lines in Figure 27) and the correlation length scales used in the retrieval process (see Equation (2.25)). The total number of travel paths can be increased simply by adding more transducer locations vertically along each tower, which will lead to better spatial resolution and slightly increase the signal processing load. Correlation length scales between velocity and temperature fluctuations are limited by the flow physics, but resolution impacts can be mitigated by accurately estimating the appropriate length scales from in situ measurements as part of the data processing.

One of the main challenges associated with orienting the interrogation area in a vertical plane will be alignment with the atmospheric flows being measured. As with the current 2D system design, the utility-scale AT system will only be able to resolve the in-plane components of the turbulent atmospheric velocity field. Because the atmospheric flow is not likely to be parallel to the interrogation area most of the time, the NREL research team will need to work to quantify measurement accuracy or fidelity losses with out-of-plane flows.

5.2.3 Applications

Scaling the AT system up for utility-scale turbines will result in snapshots of the fluctuating velocity and temperature fields at a resolution that is out of reach of existing remote sensing and in situ measurement systems. Validation efforts for high-fidelity modeling in wind energy, such as the ExaWind simulation stack (Sprague et al. 2020), repeatedly run into limits of measurement resolution and fidelity, halting or slowing progress in model application and uptake across a wide range of applications. Uncertainty that remains in high-fidelity modeling tools propagates into engineering and surrogate models used for control, optimization, and design. High-fidelity models are often used to calibrate analytical and engineering models.

A utility-scale AT system paired with an appropriate retrieval process should be able to resolve coherent structures in close proximity to the turbine blades. Many of the flow features in the near wake directly following the turbine have been explored in a purely numerical sense. The coherent turbulence seen in large-eddy simulations cannot be directly measured with existing technology. Instead, structures like tip vortices and boundary layers are inferred from related quantities (e.g., blade pressure and velocity measurements) or through flow visualization media (e.g., smoke or snow).

One of the main challenges in applying the AT system to other turbines will be the effort involved in erecting towers and instrumenting them with acoustic sensors and data acquisition systems. Tilt-up towers provide some flexibility in terms of application on location, but would account for the majority of the installation costs or system setup. An alternative to supporting transducers and data acquisition on towers is to support acoustic transducers on a combination of uncrewed aerial systems (UAS) and ground stations, explored in greater detail in Section 5.3.

5.3 Hybrid Aerial/Ground System

Supporting the speakers and microphones that define the AT system with a combination of aerial and ground stations increases the volume of the interrogation area to a scale appropriate for wind energy applications. This also allows users the flexibility to define the interrogation area for each particular application and to tune the location of each acoustic transducer for optimal travel path coverage. This minimizes flow field reconstruction error and uncertainty. Hybrid AT will advance the flow measurement state of the art for wind energy science and can be translated to a large range of other industrial flow problems related to energy, transportation, and climatology.

The feasibility of utilizing a UAS system for reconstructing turbulent velocity and temperature fields in the atmosphere has already been explored in previous studies (see Finn and Rogers 2015, 2016; Rogers and Finn 2021). Finn and Rogers (2015) deployed a UAS at an altitude of 500 m over a system of five microphones spanning 375 m. The sound of the UAS engine was used as the source. The UAS was equipped with meteorological sensors to measure temperature and velocity for comparison with the AT reconstruction. The initial results of the reconstructions were promising in light and moderate wind conditions. This study was expanded in 2021 with the use of an electric UAS outfitted with a speaker for the emission of chirps for the acoustic reconstruction, GPS for location tracking, and appropriate wind speed and temperature sensors for validation purposes. The hexicopter is shown in Figure 30. The UAS was flown over a vineyard in Australia covering a 200-m × 300-m area equipped with a total of 35 microphones as well as four weather stations at each corner of the tomographic area. The stations recorded horizontal wind speeds, temperature, humidity, and pressure. Preliminary analysis showed that the UAS reconstruction can estimate temperature with a standard error of 0.75°C and the wind velocity with an error of 0.92 m/s. With multiple UAS systems and therefore increased spatial resolution due to a greater density of travel paths, the reconstruction of turbulence fields in the wake region of a utility-scale wind turbine may be feasible.

5.3.1 Equipment

The hybrid AT system will require a swarm of at least eight UAS to resolve three-dimensional fluctuating velocity and temperature fields, such as the one implemented in the Rogers and Finn (2021) study. The hybrid aerial/ground

AT system will be built from ground-based or aerial subsystems that include co-located speaker/driver pairs, microphones, auxiliary atmospheric measurements (sonic anemometers or pressure-temperature-humidity probes), and data acquisition subsystems. Figure 31 shows a recent example of an aerial measurement platform integrated into an AT system. Subcomponents of the overall data acquisition system will be disciplined to a GPS clock and coordinates and feed directly into the processing software to estimate signal travel times; a necessary step in the fluctuating field retrieval. If GPS does not prove to be sufficiently accurate to locate the UASs, a stereo or multistatic video optical tracking system will be added to pinpoint UAS positions in 3D space. Ground stations will include microphones and speakers as well as compact data acquisition systems that can operate remotely. Portable ground weather stations will also be necessary for validation of point measurements such as those utilized in the Rogers and Finn (2021) study.

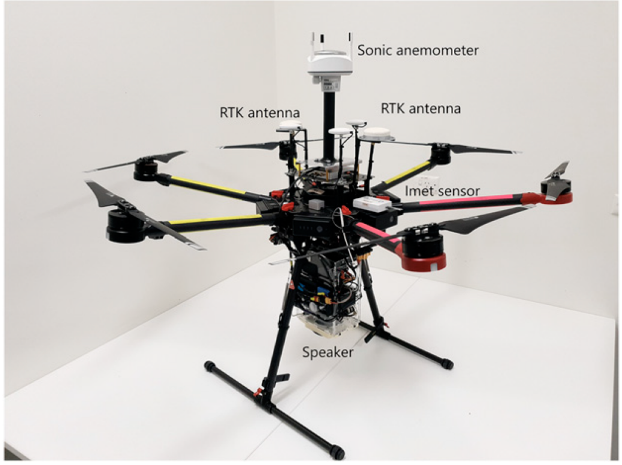

Figure 30. Hexacopter used in the Rogers and Finn (2021) UAS study.

5.3.2 Engineering Challenges

Exploratory prototypes of AT have relied on a homogeneous covariance model for the turbulent velocity and temperature fields. Previous applications of AT with UAS systems (Finn and Rogers 2015, 2016) have had to include boundary layer profiles of wind speed and temperature estimated a priori to account for vertical acoustic signal propagation characteristics. Posing the tomographic reconstruction problem as a state-estimation process, the observed acoustic signal travel times and modeled turbulent fluctuations can be leveraged together in a Kalman filter. This produces a system that describes the flow state (velocity and temperature fields) in the interrogation area. Model and retrieval algorithm advancements will be prototyped with high-fidelity models using the ExaWind simulation stack (Sprague et al. 2020).

Developing a fleet of instrumented UAS to support acoustic transducers and communication hardware will be critical for advancing the AT methodology from controlled tests to a technology that can be commercialized. This effort will specify and develop the instrument payloads, communication strategies, and flight dynamics of the UAS swarm, central to this remote sensing technology. With advances in compressed sensing methods, the locations of each UAS in space can be optimized to resolve turbulent structures of interest and to minimize measurement uncertainty and reconstruction error.

This work combines mature theories and technologies from several fields into a new technology for remote fluid measurement and classification. The key technical risks come in integrating multiscale turbulence covariance modeling methods with UAS swarm technology. The inverse problem describing the velocity and temperature fields with a collection of acoustic signal travel times relies on the precise locations of the measurement stations—a challenge that will require careful design of the UAS swarm coordination methodologies. Disciplining the subcomponents of the distributed data acquisition system to GPS for location and time synchronization may not prove to be sufficiently precise to produce accurate retrievals of atmospheric flow quantities. If that proves to be the case, additional location systems (e.g., optical tracking) may be explored to complement the hybrid system.

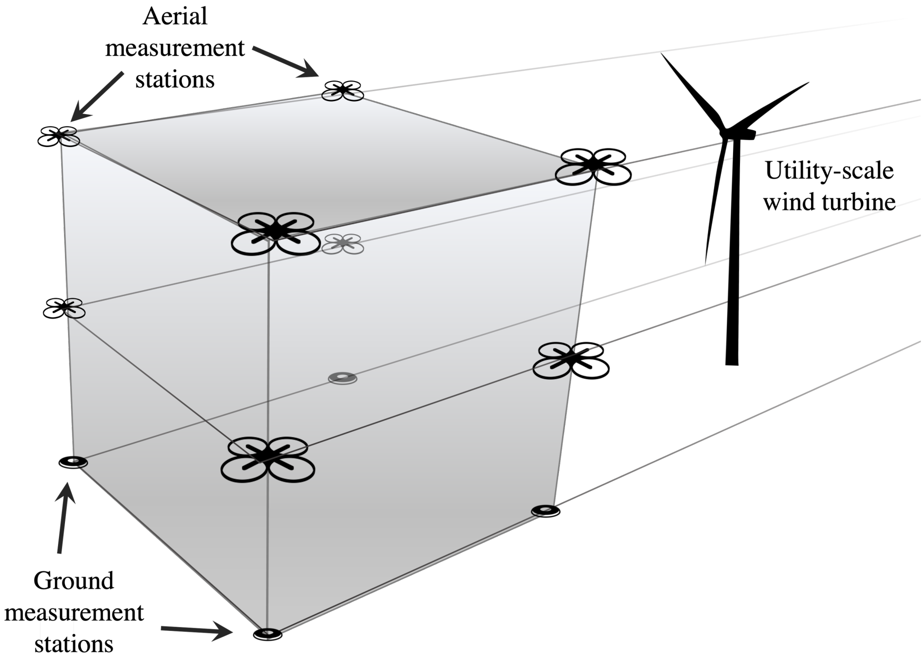

Figure 31. Three-dimensional application of the hybrid aerial/ground AT system upstream of a utility-scale turbine.

5.3.3 Applications

A hybrid aerial/ground-based system for acoustic tomography is perhaps the most flexible area for application of the measurement system. Because the system does not rely on fixed structures to support acoustic transducers, it can be reconfigured with minimal effort to suit the particular measurement needs for a wide range of applications. For renewable energy research, an aerial system will allow researchers to position acoustic transducers in areas that are unreachable with fixed-location devices, including near turbine structures or far above turbine blades. UAS-supported acoustic transducers could also be grouped in higher densities in locations where measurements are desired; the flexible arrangement allows researchers to place acoustic travel paths directly in areas of interest. This would increase the measurement density, accuracy, and resolution for specific measurement domains. Flexible sensor positions will also allow researchers to target specific phenomena of interest, such as coherent turbulent structures shed by the blades, towers, or nacelles of utility-scale wind turbines.

With an aerial system, sensor placement can be configured dynamically. Dynamic sensor placement would allow measurements to be optimized for minimal error or uncertainty during the course of a measurement period. Processing algorithms for retrieving turbulent velocity and temperature fields will need to be developed specifically to target dynamic sensor placement and optimization, provided that suitable objective functions exist to clearly determine optimal sensor locations. An AT system configuration that does not rely on towers or other structures to support transducers means that it is much easier to add or remove acoustic transducers as necessary. Ground stations comprising microphones and speakers will be inexpensive to configure and add to the system. UASs, and more likely swarm dynamics, will be the limiting factor on airborne measurement stations. However, once systems are designed, adding or removing individual UASs and measurement stations should be straightforward.

Classification of atmospheric conditions relevant to wind energy production requires insight into the fluctuating velocity field over a range of scales as well as heat and moisture fluxes. Identifying and isolating acoustic signals used for AT relies on sophisticated and efficient signal processing methods. Along with the reconstruction of the fluctuating velocity and temperature fields, coherent turbulent structures can be identified, classified, and integrated into a model-predictive control scheme for downstream wind turbines with a streaming decomposition algorithm. With a continuous updating scheme, real-time inflow information can be used to derive the optimal set point of a dynamic control strategy.

5.4 Plant-Scale System

At the extreme scale for acoustic tomography, wind plant applications stand to gain insight from flow field estimates to quantify wake losses. AT offers near-real-time flow estimates for control and for continuous monitoring. In an AT system at wind plant scale, the acoustic transducers will be supported directly on wind turbine nacelles, turning the wind plant itself into an AT array. Figure 32 shows the acoustic travel paths formed by neighboring turbines with green arrows. White boxes indicate subregions for which fluctuating flow fields can be estimated through the TDSI or other field inversion methodology.

Figure 32. Wind-plant-scaled AT array supporting acoustic transducers on wind turbine nacelles. White regions indicate nested and overlapping retrieval areas.

5.4.1 Engineering Limits

While the wind-plant-scale AT system is certainly an attractive option for large-scale flow monitoring, it also presents a significant technical challenge in terms of signal transmission, resolution, and fidelity. The audible frequency range of acoustic signals is the range least attenuated by the atmosphere—this is the reason that the acoustic signals in the existing array have particular characteristics (1.2 kHz central frequency, 700 Hz half-bandwidth). For transmission distances on the orders of kilometers, however, estimated based on a rotor diameter of 100 m and 7–10 rotor diameter separation in the wind plant, signals will require 2–4 s to transit between transducers. This limits the temporal resolution of the retrieved fields. Temporal resolution can be addressed through targeted acoustic signal redesign to vary central frequencies, bandwidths, and duration (noted in Section 5.2). Special care will have to be taken in the signal processing effort for the wind plant scale. The spatial resolution of the system will depend on the density of acoustic travel paths between turbine-mounted measurement stations, correlation length scales in the retrieval method, and assumptions in the model used by the TDSI method. As shown in Figure 32, the density of travel paths will not be uniform for most wind plants, given the variability in turbine spacing. While the temporal and spatial resolution of the wind plant scale system will likely be comparable to that of scanning lidar, the main advantage of a wind plant-scale AT array will be that snapshots of velocity can be collected throughout the domain without losses due to line of sight projections or finite scan head movement speeds.

During their travel, acoustic signals will also interact with turbulent structures in the wind plant flows. The effects of signal distortion are already visible in the subscale AT system at Flatirons Campus as a smearing of the signals in both the time and frequency domains. Although spectral broadening (frequency domain distortion) is well-documented in the literature (Ostashev et al. 2019), it amounts to convolution of the designed/emitted signal with a stochastic turbulence field along each flight path. No reliable deconvolution methods exist to support received signal filtering.

5.4.2 Regulatory Limits

As compared to a subscale system, the transmission of acoustic chirps over distances on the plant-scale system will require a significant increase in power for each signal transmission. This is likely to result in acoustic chirps exceeding regulatory limits for sound intensity. Changing the chirps such that their central frequencies are outside of the audible range would require more power per signal, corresponding to greater signal attenuation by the atmosphere. Use of a utility-scale AT system is likely to be constrained by local limitations or regulations on acoustic sound intensity, time of day, and environmental restrictions.

5.4.3 Applications

The central application of a plant-scale AT system would be for near-real-time monitoring of flow in wind plants, for which no other technologies exist. Although the acoustic travel paths within the wind plant example shown in Figure 32 are fairly sparse with path separation as high as several hundred meters, combining the field retrieval method with a wind plant flow model as with a Kalman filter will provide real-time flow estimates throughout the wind plant. The plant-scale AT system would allow wind plant owners/operators to quantify wake losses in real time under the full range of operating conditions experienced by the wind plant. Real-time flow monitoring in a wind plant represents a step-change in operational intelligence and will offer new inputs for model predictive control strategies and optimization.

5.5 Miniature Acoustic Tomography Array

The fundamental operating principle of the acoustic travel-time tomography technology is similar to that of a sonic anemometer—at least through the bulk flow quantity estimation in the linear system given by Equation (2.5). From this point of view, there could be a wide range of applications of the technology at smaller scales to make flow and temperature field observations at the component scale. The above AT system configurations discuss challenges and benefits of scaling the technology up to support flow observations for utility-scale applications. Miniaturizing the AT system would allow it to be mounted directly on blade surfaces (Figure 33) to make blade local measurements in quasi-2D configurations or virtual surfaces that follow blade geometries.

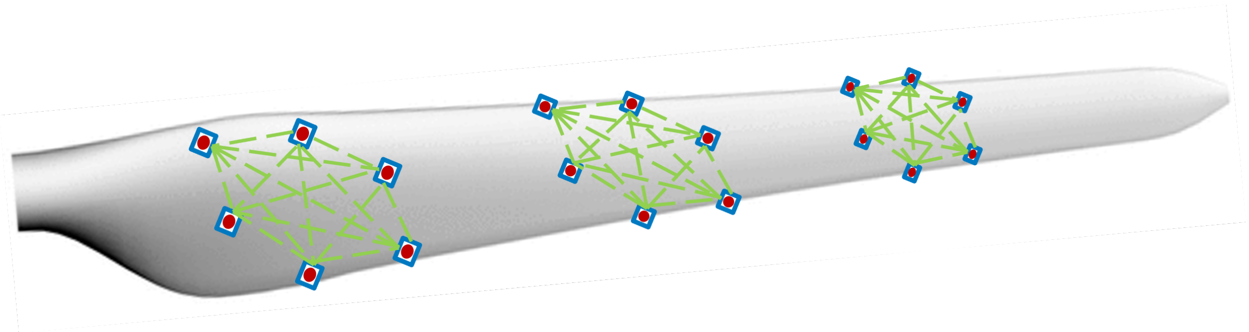

Figure 33. Miniaturized AT array surface mounted on a utility-scale wind turbine blade.

5.5.1 Engineering Challenges

Measurement systems of any type located on wind turbine blades come with a wide range of engineering and implementation challenges. Among those challenges are developing power and communications strategies that do not result in increased lightning damage risks or rotor imbalances. The precise estimation of acoustic signal travel times requires that microphones record at extremely fast sampling rates. For the subscale AT system and the utility-scale configurations detailed in this report, the nominal sampling frequencies for all microphones are set to 20 kHz. This is later upsampled by a factor of 10 for signal identification in the processing software. Sonic anemometers typically use ultrasonic frequencies to quantify velocity and speed of sound, and thus must record and process signals at much higher sampling rates. In the case of a modern sonic anemometer, signal recording and processing occur on board, and only derived velocity and speed of sound measurements are output by the system. The processing load is much higher for a miniature AT array, however, with an objective to retrieve fluctuating fields of velocity and temperature rather than a single, spatially averaged estimate. It is unlikely that a blade-mounted system would have the processing capability needed to produce field estimates onboard, and would therefore have to stream data to a central processing center. Transmitting raw acoustic data from the point of measurement to a central repository will require either a fiber-based solution and central processing computer in the hub or blade, or a high-bandwidth wireless communication to a processing station on the ground.

Powering the system will incur similar challenges. While the acoustic signals will require little power to cover small distances, the speaker drivers, microphones, and data acquisition systems are all powered subsystems. Long copper cable runs in blades can significantly increase risks of lightning strikes and associated damages and are typically discouraged by turbine manufacturers and owners. Past examples of blade-mounted instruments have supplied power through battery-based solutions. Another alternative is power-over-fiber (PoF) systems, which rely on optical power as an energy source in addition to a communication system. PoF systems would likely be among the constraining factors in system designs, given that power transmission over optical fibers is typically limited to around 50 milliamps (mA). In order to leverage PoF systems, speakers, microphones, and data acquisition system components would all need to adhere to power availability and communication rate limits.

5.5.2 Applications

Few technologies exist to make blade local flow observations. To date, the most successful observations of wind speed near wind turbine blades have used classic measurement technology such as pitot or five-hole probes. These probes require pressure transducers and ancillary equipment, or tufts, which provide wind direction and boundary layer separation information, but struggle to provide quantitative wind velocity vector data. Surface-mounted AT measurements could easily be made to collect data in 2D planes or to conform to blade geometries simply by adjusting sensor heights off the blade surface. Snapshots of the fluctuating velocity fields within the blade boundary layer would be an unprecedented advancement of measurement technology that would significantly improve our fundamental understanding of blade-local flows. Observations from miniaturized or blade-mounted AT systems would bring airfoil design and performance validation out of the wind tunnel setting and into practical environments. The same measurements could be used to validate boundary layer separation and static/dynamic stall behavior of operating wind turbines, which is a major source of uncertainty for all blade resolving computational fluid dynamics simulations of wind turbines.

6 Discussion and Conclusions

Wind energy flows are a subject of continued interest due to the complex aerodynamic interactions of the wind turbine rotors with the ABL. Wind power is a maturing technology, but the fundamental aerodynamics of wind energy continues to be the subject of research with respect to design optimization. Modest gains in turbine aerodynamic performance can lead to substantial improvements in the energy production and added value due to the number of turbines installed worldwide. Fundamental questions remain open regarding the evolution of wind turbine wakes under wake-steering strategies, the behaviors of wakes in varying thermodynamic states of the ABL as well as over complex terrain, as outlined by Meneveau (2019). The ability to remotely access velocity and temperature fields at high resolution will enable the wind energy research community to address many questions about wake formation and evolution and energy entrainment and dissipation.

Acoustic tomography is a promising and innovative remote sensing technology for collecting observations of wind energy flows. It offers an alternative to current remote sensing technologies and provides the means to simultaneously reconstruct spatially and temporally resolved fluctuating velocity and temperature fields within a volume of interest. This technique has the potential to advance our understanding of the flows incident on wind turbines, wakes, and fundamental transport mechanisms between ground and atmosphere. The AT array installed at the Flatirons Campus is unique to NREL and will advance understanding of turbulent flow near wind turbines and in wind plants, which is critical for design, optimization, and model validation.

Atmospheric processes are of critical importance in a wide range of fields that include weather prediction, land-atmosphere exchange of heat and moisture, agriculture, and local climate research. Accessing field information in the turbulent ABL is necessary to address questions around many physical processes and to provide a means for model validation. Currently, instruments used to perform field experiments fall short of providing the necessary resolution in time and space to resolve turbulent flow and temperature scales. There is a growing need for an economical remote sensing technology for the study of multidimensional coherent structures and very stable boundary layers, and for characterizing turbulent flow in complex terrain (Arnold, Ziemann, and Raabe 1999; D. Wilson et al. 2001; D. K. Wilson et al. 2004).

The existing AT array at NREL has been used to test the viability of the 2D AT method for atmospheric flows. This array can be outfitted with additional acoustic transducers to resolve turbulent flow structures in 3D volumes. This will not only facilitate the potential resolution of the wake of the subscale wind turbine within the array, but also lead to potential advancements in the study of atmospheric processes in the ABL. Characterizing the AT array is a critical step in identifying and accounting for sources of uncertainty in the measurement chain. Discussed in Section 3, the collection of signal emission from nonpoint source speakers and detection delays in the hardware lead to a 3.5%–10% error in travel time estimation, verified through the self-calibration procedure. By comparison, the normal error seen in the preliminary measurements of the bulk flow (e.g., $\mathrm{std}(u)/u_0$) is on the order of 1.5%. Measurement uncertainty from the signal processing part of AT is collected into the noise term that describes higher-order terms from linearizing the relationship between travel time and the thermodynamic/mechanical state of the atmosphere. The NMSE of the TDSI process is on the order of 35%–54%—clearly indicating that the greatest part of the uncertainty is in the fluctuating field estimates.

AT technology can be scaled to resolve flows around utility-scale turbines. NREL already has the infrastructure in place to mount transducers and receivers on existing meteorological towers, allowing the interrogation of vertically-oriented 2D planes of turbulence around a wind turbine. A utility-scale system may also be able to resolve coherent turbulent structures in close proximity to a wind turbine, a capability that is out of reach with other remote sensing and in situ measurement technologies. Another possible AT system configuration includes the implementation of a hybrid aerial/ground system that would allow researchers to flexibly locate acoustic transducers to dynamically target flow structures of interest.

For AT system configurations of all scales, there are many factors that could ultimately impact resolution, measurement errors and uncertainty. Intuitively, the number of acoustic travel paths crossing the interrogation area, the design of acoustic chirps, the sampling frequency of the system (i.e., frames per second), and the covariance model all impact measurement error. However, no clear dependence of error on any of these factors is easily found in the literature. A detailed error assessment and uncertainty quantification is one of the key priorities for future systems that will inform capabilities of future designs. As time-of-flight measurement systems like AT are inherently different than line-of-sight systems like lidar, direct comparisons of capabilities are difficult. Table 5 compares characteristics of commercial lidar technology to those of the AT system configurations explored in Section 5.

Table 5. Comparison of measurement range and resolution for AT system configurations and commerically-available scanning lidar

	Spatial resolution (m)	Maximum range (m)	Temporal resolution (s)	Scan time (s)
2D AT array	1.5	100	0.05-0.5	—
3D AT array	1.5	100	0.1–2	—
Utility scale (tower)	5–10	500	1.5–3.5	—
Hybrid AT array	2–10	300	1.5–3.5	—
Plant scale AT array	30–50	1,000	3–8	—
Miniature AT array	0.03–0.1	3	0.01–0.1	—
Scanning lidar	15–30	1,000–5,000	6–12	180–270

References

Aitken, M. L., and J. K. Lundquist. 2014. “Utility-Scale Wind Turbine Wake Characterization Using Nacelle-Based Long-Range Scanning Lidar.” *Journal of Atmospheric and Oceanic Technology* 31 (7): 1529–1539.

Arnold, K., A. Ziemann, and A. Raabe. 1999. “Acoustic tomography inside the atmospheric boundary layer.” *Physics and Chemistry of the Earth, Part B: Hydrology, Oceans and Atmosphere* 24 (1-2): 133–137.

Finn, A., and K. Rogers. 2015. “The feasibility of unmanned aerial vehicle-based acoustic atmospheric tomography.” *The Journal of the Acoustical Society of America* 138 (2): 874–889.

———. 2016. “Improving unmanned aerial vehicle–based acoustic atmospheric tomography by varying the engine firing rate of the aircraft.” *Journal of Atmospheric and Oceanic Technology* 33 (4): 803–816.

Hamilton, N., and M. C. Debnath. 2019. *National Wind Technology Center-Characterization of Atmospheric Conditions.* Technical report. National Renewable Energy Lab.(NREL), Golden, CO (United States).

Herges, T. G., D. C. Maniaci, B. T. Naughton, T. Mikkelsen, and M. Sjöholm. 2017. “High resolution wind turbine wake measurements with a scanning lidar.” *Journal of Physics: Conference Series* 854 (May): 012021.

Iungo, G. V., and F. Porté-Agel. 2014. “Volumetric Lidar Scanning of Wind Turbine Wakes under Convective and Neutral Atmospheric Stability Regimes.” *Journal of Atmospheric and Oceanic Technology* 31 (10): 2035–2048.

Kamrath, M. J., V. E. Ostashev, D. K. Wilson, M. J. White, C. R. Hart, and A. Finn. 2021. “Vertical and slanted sound propagation in the near-ground atmosphere: Amplitude and phase fluctuations.” *The Journal of the Acoustical Society of America* 149 (3): 2055–2071.

Mann, J., A. Peña, F. Bingöl, R. Wagner, and M. S. Courtney. 2010. “Lidar Scanning of Momentum Flux in and above the Atmospheric Surface Layer.” *Journal of Atmospheric and Oceanic Technology* 27 (6): 959–976.

Maric, E., and N. Hamilton. 2023. “Acoustic Travel-Time Tomography for Wind Energy.” In *AMS 24th Symposium on Boundary Layers and Turbulence Meeting Abstracts.*

Meneveau, C. 2019. “Big wind power: seven questions for turbulence research.” *Journal of Turbulence* 20 (1): 2–20.

Ostashev, V. E., A. J. Bedard, S. N. Vecherin, and D. K. Wilson. 2008. “Acoustic tomography of the atmosphere at the Boulder Atmospheric Observatory.” *The Journal of the Acoustical Society of America* 124 (4): 2591–2591.

Ostashev, V. E., S. N. Vecherin, D. K. Wilson, A. Ziemann, and G. H. Goedecke. 2009. “Recent progress in acoustic travel-time tomography of the atmospheric surface layer.” *Meteorologische Zeitschrift* 18 (2): 125–133.

Ostashev, V. E., and D. K. Wilson. 2015. *Acoustics in moving inhomogeneous media.* CRC Press.

Ostashev, V. E., D. K. Wilson, A. Finn, and E. Barlas. 2019. “Theory for spectral broadening of narrowband signals in the atmosphere and experiment with an acoustic source onboard an unmanned aerial vehicle.” *The Journal of the Acoustical Society of America* 145 (6): 3703–3714.

Rogers, K. J., and A. Finn. 2021. “Methodology Improvements for Three-Dimensional UAV-Based Travel-Time Acoustic Atmospheric Tomography.” *Journal of Atmospheric and Oceanic Technology* 38 (12): 2147–2163.

Schroeder, J., B. Hirth, and J. Guynes. 2017. *Final Technical Report: The Incubation of Next-Generation Radar Technologies to Lower the Cost of Wind Energy.* Technical report. Texas Tech Univ., Lubbock, TX (United States).

Sprague, M. A., S. Ananthan, G. Vijayakumar, and M. Robinson. 2020. “ExaWind: A multifidelity modeling and simulation environment for wind energy.” In *Journal of Physics: Conference Series,* 1452:012071. 1. IOP Publishing.

Vecherin, S. N., V. E. Ostashev, G. H. Goedecke, D. K. Wilson, and A. G. Voronovich. 2006. “Time-dependent stochastic inversion in acoustic travel-time tomography of the atmosphere.” *The Journal of the Acoustical Society of America* 119 (5): 2579–2588.

Vecherin, S. N., V. E. Ostashev, and D. K. Wilson. 2008. “Three-dimensional acoustic travel-time tomography of the atmosphere.” *Acta Acustica united with Acustica* 94 (3): 349–358.

Wilson, D. K., V. E. Ostashev, S. N. Vecherin, A. G. Voronovich, S. L. Collier, and J. M. Noble. 2004. “Assessment of Acoustic Travel-Time Tomography of the Atmospheric Surface Layer.”

Wilson, D., A. Ziemann, V. Ostashev, and A. Voronovich. 2001. “An overview of acoustic travel-time tomography in the atmosphere and its potential applications.” *Acta Acustica united with Acustica* 87 (6): 721–730.